



Evidence for Jet/Outflow Shocks Heating the Environment around the Class I Protostellar Source Elias 29: FAUST XXI

Yoko Oya¹ , Eri Saiga², Anna Miotello³, Maria Koutoulaki⁴, Doug Johnstone^{5,6}, Cecilia Ceccarelli⁷, Claire J. Chandler⁸ , Claudio Codella^{7,9}, Nami Sakai¹⁰, Eleonora Bianchi¹¹ , Mathilde Bouvier¹², Steven Charnley¹³, Nicolas Cuello⁷, Marta De Simone^{3,9}, Logan Francis¹⁴, Tomoyuki Hanawa¹⁵ , Izaskun Jiménez-Serra¹⁶, Laurent Loinard^{17,18,19}, Francois Menard⁷, Giovanni Sabatini⁹, Charlotte Vastel²⁰, Ziwei Zhang¹⁰, Yuri Aikawa²¹ , Felipe O. Alves²², Nadia Balucani²³, Gemma Busquet^{7,24}, Paola Caselli²², Emmanuel Caux²⁰, Spandan Choudhury²², Francois Dulieu²⁵ , Aurora Durán²⁶, Lucy Evans^{9,20}, Davide Fedele^{9,27}, Siyi Feng²⁸, Francesco Fontani^{9,22}, Tetsuya Hama^{29,30}, Eric Herbst³¹, Shingo Hirano²¹, Tomoya Hirota^{32,33}, Andrea Isella³⁴, Claudine Kahane⁷, Bertrand Lefloch⁷, Romane Le Gal^{7,35}, Hanyu Baobab Liu³⁶, Ana López-Sepulcre^{7,35}, Luke T. Maud³, María José Maureira²², Seyma Mercimek³⁷, George Moellenbrock⁸, Shoji Mori²¹, Hideo Nomura³⁸, Yasuhiro Oba³⁹, Ross O'Donoghue⁴⁰, Satoshi Ohashi³², Yuki Okoda¹⁰, Juan Ospina-Zamudio⁷, Jaime Pineda²², Linda Podio⁹, Albert Rimola⁴¹, Takeshi Sakai⁴², Dominique Segura-Cox²², Yancy Shirley⁴³, Brian Svoboda⁴⁴, Leonardo Testi^{3,9}, Serena Viti⁴⁴, Naoki Watanabe³⁹, Yoshimasa Watanabe⁴⁵, Yichen Zhang⁴⁶, and Satoshi Yamamoto^{47,48}

¹ Center for Gravitational Physics, Yukawa Institute for Theoretical Physics, Kyoto University, Oiwake-cho, Kitashirakawa, Sakyo-ku, Kyoto-shi, Kyoto-fu 606-8502, Japan; yoko.oya@yukawa.kyoto-u.ac.jp

² Department of Physics, The University of Tokyo, 7-3-1, Hongo, Bunkyo-ku, Tokyo 113-0033, Japan

³ European Southern Observatory, Karl-Schwarzschild Str. 2, 85748 Garching bei München, Germany

⁴ School of Physics & Astronomy, University of Leeds, Woodhouse Lane, LS2 9JT Leeds, UK

⁵ NRC Herzberg Astronomy and Astrophysics, 5071 West Saanich Road, Victoria, BC, V9E 2E7, Canada

⁶ Department of Physics and Astronomy, University of Victoria, Victoria, BC, V8P 5C2, Canada

⁷ Université Grenoble Alpes, CNRS, IPAG, 38000 Grenoble, France

⁸ National Radio Astronomy Observatory, PO Box O, Socorro, NM 87801, USA

⁹ INAF, Osservatorio Astrofisico di Arcetri, Largo E. Fermi 5, I-50125, Firenze, Italy

¹⁰ RIKEN Cluster for Pioneering Research, 2-1, Hirosawa, Wako-shi, Saitama 351-0198, Japan

¹¹ Excellence Cluster ORIGINS, Boltzmannstraße 2, 85748, Garching bei München, Germany

¹² Leiden Observatory, Leiden University, P.O. Box 9513, 2300 RA Leiden, The Netherlands

¹³ Instituto de Radioastronomía y Astrofísica, Universidad Nacional Autónoma de México, 58090 Morelia, Mexico

¹⁴ Leiden Observatory, Leiden University, PO Box 9513, 2300 RA Leiden, The Netherlands

¹⁵ Center for Frontier Science, Chiba University, 1-33 Yayoi-cho, Inage-ku, Chiba 263-8522, Japan

¹⁶ Centro de Astrobiología (CAB), CSIC-INTA, Ctra. de Ajalvir, km 4, 28850, Torrejón de Ardoz, Spain

¹⁷ Instituto de Radioastronomía y Astrofísica, Universidad Nacional Autónoma de México, Apartado Postal 3-72, Morelia 58090, Michoacán, Mexico

¹⁸ Black Hole Initiative at Harvard University, 20 Garden Street, Cambridge, MA 02138, USA

¹⁹ David Rockefeller Center for Latin American Studies, Harvard University, 1730 Cambridge Street, Cambridge, MA 02138, USA

²⁰ IRAP, Université de Toulouse, CNRS, CNES, UPS, Toulouse, France

²¹ Department of Astronomy, The University of Tokyo, 7-3-1 Hongo, Bunkyo-ku, Tokyo 113-0033, Japan

²² Center for Astrochemical Studies, Max-Planck-Institut für Extraterrestrische Physik (MPE), Gießenbachstr. 1, D-85741 Garching, Germany

²³ Department of Chemistry, Biology, and Biotechnology, The University of Perugia, Via Elce di Sotto 8, 06123 Perugia, Italy

²⁴ Departament de Física Quàntica i Astrofísica, Institut de Ciències del Cosmos, Universitat de Barcelona (IEEC-UB), Martí i Franqués, 1, 08028, Barcelona, Catalunya, Spain

²⁵ CY Cergy Paris Université, Sorbonne Université, Observatoire de Paris, PSL University, CNRS, LERMA, F-95000, Cergy, France

²⁶ Instituto de Radioastronomía y Astrofísica, Universidad Nacional Autónoma de México, A.P. 3-72 (Xangari), 8701, Morelia, Mexico

²⁷ INAF, Osservatorio Astrofisico di Torino, Via Osservatorio 20, 10025, Pino Torinese, Italy

²⁸ Department of Astronomy, Xiamen University, Xiamen, Fujian 361005, People's Republic of China

²⁹ Komaba Institute for Science, The University of Tokyo, 3-8-1 Komaba, Meguro, Tokyo 153-8902, Japan

³⁰ Department of Basic Science, The University of Tokyo, 3-8-1 Komaba, Meguro, Tokyo 153-8902, Japan

³¹ Department of Chemistry, University of Virginia, McCormick Road, PO Box 400319, Charlottesville, VA 22904, USA

³² National Astronomical Observatory of Japan, Osawa 2-21-1, Mitaka-shi, Tokyo 181-8588, Japan

³³ Department of Astronomical Sciences, SOKENDAI (The Graduate University for Advanced Studies), 2-21-1 Osawa, Mitaka-shi, Tokyo 181-8588, Japan

³⁴ Department of Physics and Astronomy, Rice University, 6100 Main Street, MS-108, Houston, TX 77005, USA

³⁵ Institut de Radioastronomie Millimétrique, 38406 Saint-Martin d'Hères, France

³⁶ Institute of Astronomy and Astrophysics, Academia Sinica, 11F of Astronomy-Mathematics Building, AS/NTU No.1, Sec 4, Roosevelt Road, Taipei 10617, Taiwan, R.O.C.

³⁷ Università degli Studi di Firenze, Dipartimento di Fisica e Astronomia, via G. Sansone 1, 50019 Sesto Fiorentino, Italy

³⁸ Division of Science, National Astronomical Observatory of Japan, 2-21-1 Osawa, Mitaka, Tokyo 181-8588, Japan

³⁹ Institute of Low Temperature Science, Hokkaido University, N19W8, Kita-ku, Sapporo, Hokkaido 060-0819, Japan

⁴⁰ Department of Physics and Astronomy, University College London, Gower Street, London, WC1E 6BT, UK

⁴¹ Departament de Química, Universitat Autònoma de Barcelona, 08193 Bellaterra, Spain

⁴² Graduate School of Informatics and Engineering, The University of Electro-Communications, Chofu, Tokyo 182-8585, Japan

⁴³ Steward Observatory, 933 N Cherry Avenue, Tucson, AZ 85721, USA

⁴⁴ Leiden Observatory, Leiden University, PO Box 9513, NL02300 RA, Leiden, The Netherlands

⁴⁵ Materials Science and Engineering, College of Engineering, Shibaura Institute of Technology, 3-7-5 Toyosu, Koto-ku, Tokyo 135-8548, Japan

⁴⁶ Department of Astronomy, Shanghai Jiao Tong University, 800 Dongchuan Road, Minhang, Shanghai 200240, People's Republic of China

⁴⁷ SOKENDAI (The Graduate University for Advanced Studies), Hayama-cho, Miura-gun, Kanagawa 240-0193, Japan

⁴⁸Research Center for the Early Universe, The University of Tokyo, 7-3-1, Hongo, Bunkyo-ku, Tokyo 113-0033, Japan
Received 2024 August 14; revised 2025 January 14; accepted 2025 January 16; published 2025 February 20

Abstract

We have observed the late Class I protostellar source Elias 29 at a spatial resolution of 70 au with the Atacama Large Millimeter/submillimeter Array as part of the FAUST Large Program. We focus on the line emission of SO, while that of ^{34}SO , C^{18}O , CS, SiO, H^{13}CO^+ , and DCO^+ are used supplementarily. The spatial distribution of the SO rotational temperature ($T_{\text{rot}}(\text{SO})$) is evaluated by using the intensity ratio of its two rotational excitation lines. Besides in the vicinity of the protostar, two hot spots are found at a distance of 500 au from the protostar; $T_{\text{rot}}(\text{SO})$ locally rises to 53^{+25}_{-15} K at the interaction point of the outflow and the southern ridge, and 72^{+66}_{-29} K within the southeastern outflow probably due to a jet-driven bow shock. However, the SiO emission is not detected at these hot spots. It is likely that active gas accretion through the disk-like structure and onto the protostar still continues even at this evolved protostellar stage, at least sporadically, considering the outflow/jet activities and the possible infall motion previously reported. Interestingly, $T_{\text{rot}}(\text{SO})$ is as high as 20–30 K even within the quiescent part of the southern ridge apart from the protostar by 500–1000 au without clear kinematic indication of current outflow/jet interactions. Such a warm condition is also supported by the low deuterium fractionation ratio of HCO^+ estimated by using the H^{13}CO^+ and DCO^+ lines. The B-type star HD147889 ~ 0.5 pc away from Elias 29, previously suggested as a heating source for this region, is likely responsible for the warm condition of Elias 29.

Unified Astronomy Thesaurus concepts: [Astrochemistry \(75\)](#); [Stellar winds \(1636\)](#); [Star formation \(1569\)](#); [Low mass stars \(2050\)](#); [Protostars \(1302\)](#)

1. Introduction

1.1. Background

A wide variety of planetary systems have been discovered in recent decades (e.g., S. M. Andrews et al. 2018; K. I. Öberg et al. 2021). The origin of their diversity, both in physics and chemistry, probably resides in the earliest history of the planetary system formation, namely, what happened during the protostellar phases. Thus, it is important to investigate this phase to obtain a thorough understanding of star and planet formation and its diversity. In this phase, gas accretion to the protostar and dissipation of surrounding gas are simultaneously ongoing, so that a parent core generally reveals a very complex structure. Recent Atacama Large Millimeter/submillimeter Array (ALMA) observations have indeed delineated a detailed view of the complex physical and chemical nature of protostellar sources at a high angular resolution (e.g., K. Tokuda et al. 2014; Y. Oya et al. 2016; M. H. D. van der Wiel et al. 2019; Y. Oya & S. Yamamoto 2020; Y. Okoda et al. 2021; S. Ohashi et al. 2022; C. Codella et al. 2024). In both gas accretion and dissipation, the outflow/jet plays a central role (e.g., R. Bachiller 1996; J. Bally 2016).

First, outflows are known to be important mechanisms for removing angular momentum from the gas accreting onto the protostar, and therefore closely connected to the formation of the disk/envelope system and the growth of protostars (e.g., R. D. Blandford & D. G. Payne 1982; K. Tomisaka 2000; M. N. Machida et al. 2008; T. Hirota et al. 2017; M. N. Machida & S. Basu 2019). Second, the outflow plays a crucial role in the dissipation of the parent core, the details of which are still an open issue of theoretical study (e.g., S. S. R. Offner & J. Chaban 2017; F. Nakamura & Z.-Y. Li 2014). The outflow evolution is thus important for both regulation and feedback processes in the formation of a star and the circumstellar environment. Hence,

outflows have extensively been studied by radio observations, particularly for early-stage protostars (e.g., C.-F. Lee et al. 2000; H. G. Arce & A. I. Sargent 2006; J. Hatchell et al. 2007; E. I. Curtis et al. 2010; Y. Matsushita et al. 2019; F. Nakamura et al. 2011; Y. Oya et al. 2014, 2015, 2018b, 2018a, 2021; M. Omura et al. 2024). Furthermore, it is known that the chemical composition of a parent core is greatly affected by the outflow activity (e.g., H. Mikami et al. 1992; R. Bachiller & M. Pérez Gutiérrez 1997; R. Bachiller et al. 2001; H. G. Arce et al. 2008; C. Codella et al. 2010; C. Ceccarelli et al. 2010, 2017; M. Sugimura et al. 2011; L. Podio et al. 2017). Hence, the outflow stands for a key phenomenon to disentangle complex physical and chemical structure of protostellar cores.

On the other hand, observational studies of outflows and their feedback on the chemical evolution of evolved protostars at the late Class I stage are relatively sparse, especially at high angular resolution (e.g., R. Le Gal et al. 2020; E. Bianchi et al. 2022; M. Tanious et al. 2024). This is in part due to the lower mass accretion rates associated with evolved protostars, which generally drive less powerful and fainter outflows (e.g., M. N. Machida & T. Hosokawa 2013). Therefore, it is important to investigate additional sources at the late evolutionary stage, to attain a more thorough understanding of both the outflow evolution and its feedback to the parent core. Even if the outflow feature is faint, temperature structure as well as chemical structure around the protostar would tell us important information on the outflow activity. Moreover, accreted material at the late evolutionary stage remains in the disk and could have an outsized contribution to planets and comets. Thus, the nature of the late-accreting material would affect the chemical composition of comets; for instance, a supply of warm material could result in lower deuterium fractionation in comets than in the dense interstellar medium. Given these needs, we included the relatively evolved protostellar source Elias 29 in our ALMA large program FAUST (Fifty AU Study of the chemistry in the disk/envelope system of solar-like protostars; 2018.1.01205.L; P.I.: S. Yamamoto). FAUST aims to delineate physical and chemical structures of 13 protostellar sources at a spatial resolution of ~ 50 au (C. Codella et al. 2021; Y. Oya et al. 2025, in preparation).

⁴⁹ Jansky Fellow of the National Radio Astronomy Observatory.



1.2. Target Source: Elias 29

Elias 29, also known as WL 15 (B. A. Wilking & C. J. Lada 1983), is a Class I protostar in the L1688 dark cloud within the Ophiuchus star-forming region ($d = 137$ pc; G. N. Ortiz-León et al. 2017). D. Lommen et al. (2008) reported a bolometric temperature and bolometric luminosity of 391 K and $13.6 L_{\odot}$, respectively. The systemic velocity of the protostellar system is about 4 km s^{-1} (Y. Oya et al. 2019). Elias 29 is surrounded by many YSOs, making the environment of this source very complex (W. R. M. Rocha & S. Pilling 2018).

Previous observational studies of Elias 29 at $>10^4$ au scale have focused on its outflow structure (Y. Sekimoto et al. 1997; C. Ceccarelli et al. 2002; R. S. Bussmann et al. 2007; J. E. Ybarra et al. 2006; F. Nakamura et al. 2011; N. van der Marel et al. 2013). According to CO ($J = 3 - 2$) observations with Heinrich Hertz Telescope by R. S. Bussmann et al. (2007), the outflow has an inverse S-like shape at a 4000 au scale. The S-like structure is presumably due to a temporal change in the outflow direction. On a smaller scale around the protostar, C. Ceccarelli et al. (2002) detected the outflow in CO ($J = 6 - 5$) emission with the James Clerk Maxwell Telescope, noting that the blueshifted and redshifted lobes are on the west and east sides of the protostar, respectively. In addition, the protostellar jet was observed in the near-infrared by J. E. Ybarra et al. (2006), revealing H_2 knots produced by the precessing east–west jet, consistent with the outflow morphology found by C. Ceccarelli et al. (2002) and R. S. Bussmann et al. (2007).

The gas structures observed in Elias 29 at $<10^3$ au scale consist of two main components, according to the observations of various molecular lines by D. Lommen et al. (2008) and Y. Oya et al. (2019). These are a compact central component associated to the protostar and an off-center dense gas clump (called the “southern ridge” hereafter). The southern ridge is ~ 500 au ($\sim 4''$) south of the protostar and extends along the northeast–southwest direction, and its origin is unclear at the moment (D. Lommen et al. 2008; Y. Oya et al. 2019). Y. Oya et al. (2019) observed Elias 29 in SO and SO_2 emission with ALMA, reporting rotational motion for the compact component associated to the protostar. The authors estimated the protostellar mass to be from 0.8 – $1.0 M_{\odot}$, assuming Keplerian motion, and a disk inclination angle from 65° – 90° (0° for face-on).

The molecular gas within Elias 29 is reported to show peculiar chemical characteristics (Y. Oya et al. 2019). According to their results, the SO and SO_2 emission is very bright in the compact component around the protostar. The compact distribution of SO_2 in this source has also been reported by E. Artur de la Villarmois et al. (2019). Such compact distributions of SO and SO_2 have been reported for a few other sources (e.g., SVS 13 by C. Codella et al. 2021 and E. Bianchi et al. 2023; Oph IRS 44 by E. Artur de la Villarmois et al. 2022). On the other hand, CS emission (which, for systems with typical chemical characteristics, is usually bright within the disk/envelope system; e.g., Y. Oya et al. 2015, 2017; M. Imai et al. 2016) is faint toward the continuum peak and is preferentially seen within the southern ridge. Both of the components are deficient in interstellar complex organic molecules (iCOMs), such as HCOOCH_3 and $(\text{CH}_3)_2\text{O}$, and unsaturated hydrocarbon molecules, such as CCH and $\text{c-C}_3\text{H}_2$. As a possible explanation for these chemical characteristics, Y. Oya et al. (2019) proposed a relatively high dust temperature (≥ 20 K) in the parent cloud; dust surface reactions to form the above molecular species would be insufficient

because such a high dust temperature prevents their mother species (e.g., C and CO) from depletion onto dust grains (see Section 5.2; Y. Oya 2022). Indeed, W. R. M. Rocha & S. Pilling (2018) reported that the parent cloud of Elias 29 is irradiated by two bright BV stars, S1 and HD 147889; their model calculation suggested that the gas temperature of the cloud should not have been below 20 K. The actual temperature in the environment around the protostar, however, has not been delineated observationally so far; therefore, we first delineate the temperature distribution in Elias 29 at a 10^2 – 10^3 au scale in this project.

In this paper, we focus on the distribution of the rotational temperature of SO by using two SO lines in ALMA Band 6. The details of the observations are given in Section 2. Section 3 describes the overall view of the observational results, including the findings of hot regions. The hot regions are also found to be characteristic in gas dynamics (Section 4); we discuss the feedback induced by the outflow (Section 4.1) and jet (Section 4.2) activities in this source as the candidate cause for the local heating of the gas apart from the protostar. The mass accretion is discussed in Section 4.3. The chemical composition of this source is explored in Section 5. The SO column density is evaluated in Section 5.1 and found not to be significantly enhanced by the shock chemistry. As a support for the warm environment of this source, the deuterium fractionation ratio of HCO^+ is discussed by using the H^{13}CO^+ and DCO^+ emissions in Section 5.2. Section 6 provides a summary of this paper.

2. Observation

With ALMA, we observed the field around Elias 29 between 2018 October and 2020 March during Cycle 6 operation, as part of the ALMA large program FAUST (2018.1.01205.L). Spectral lines listed in Table 1 were observed in Band 6 using two frequency ranges, Setup 1 (214.0–219.0 GHz, 229.0–234.05 GHz) and Setup 2 (242.5–247.5 GHz, 257.5–262.5 GHz). In each spectral setup, we used the 12 m array data with two different antenna configurations, C43-4 and C43-1, as well as the 7-m array data of the Atacama Compact Array (ACA/Morita Array). Both Setups 1 and 2 were observed by 12 spectral windows with the bandwidth and the frequency resolution of 59 MHz and 122 kHz (0.15 km s^{-1} at 250 GHz), respectively, and one with the bandwidth and the frequency resolution of 1875 MHz and 1.129 MHz (1.4 km s^{-1} at 250 GHz), respectively. The basic parameters of the observations including calibrator sources are summarized in Table 2. The field center of the observations was $(\alpha_{\text{ICRS}}, \delta_{\text{ICRS}}) = (16^{\text{h}}27^{\text{m}}09^{\text{s}}.437, -24^{\circ}37'19''.304)$.

The system temperature (T_{sys}) was typically 70–130 K during the observations. The data were reduced using the Common Astronomy Software Applications (CASA) package (CASA Team et al. 2022) utilizing a modified version of the ALMA calibration pipeline based on v.5.6.1-8.e17 and an additional in-house calibration routine to correct for the T_{sys} and spectral line data normalization.⁵⁰ Self-calibration was carried out using line-free continuum emission for each configuration. Details of the self-calibration process are described by M. Imai et al. (2022). The visibility data with the three different configurations were combined in the UV plane after the self-calibration. The absolute accuracy of the

⁵⁰ <https://faust-imaging.readthedocs.io/en/latest/>

Table 1
List of the Observed Lines^a

Molecule	Frequency (GHz)	S_{μ}^2 (D ²)	E_u (K)	Beam Size ^b	rms (mJy beam ⁻¹)
C ¹⁸ O ($J = 2 - 1$)	219.5603541	0.0244	16	0 ^h 531 × 0 ^h 438 (P.A. -89°463)	1.8
SO ($J_N = 6_5 - 5_4$)	219.949442	14.0	35	0 ^h 528 × 0 ^h 435 (P.A. 89°739)	2.3 ^c
SO ($J_N = 6_6 - 5_5$)	258.2558259	13.7	57	0 ^h 573 × 0 ^h 451 (P.A. -79°952)	2.5 ^c
³⁴ SO ($J_N = 5_6 - 4_5$)	246.66347	11.4	50	0 ^h 518 × 0 ^h 392 (P.A. -73°648)	1.3
CS ($J = 5 - 4$)	244.9355565	19.2	35	0 ^h 523 × 0 ^h 402 (P.A. -73°669)	1.8
SiO ($J = 5 - 4$)	217.1049190	48.0	31	0 ^h 537 × 0 ^h 439 (P.A. -88°865)	1.7
H ¹³ CO ⁺ ($J = 3 - 2$)	260.255339	45.6	25	0 ^h 497 × 0 ^h 381 (P.A. -73°099)	2.8
DCO ⁺ ($J = 3 - 2$)	216.1125822	45.6	21	0 ^h 540 × 0 ^h 442 (P.A. -88°636)	2.3

Notes.

^a Taken from CDMS (H. S. P. Müller et al. 2005; C. P. Endres et al. 2016).

^b Synthesized beam.

^c rms noise of the data with the beam size of 0^h6 × 0^h6.

Table 2
Observation Parameters

	Configuration	Date	T_{target} (min)	N _{Antennas}	Baseline (m)	MRS ^a (arcsec)	Calibrator		
							Phase	Bandpass	Flux
Setup 1	C43-4	2018 Dec 2	29.35	43	15.1–783.5	5.7	J1625–2527	J1427–4206	J1427–4206
	C43-4	2019 May 4	29.35	40	15.1–740.4	5.5	J1626–2951	J1427–4206	J1427–4206
	C43-4	2020 Mar 16	29.33	44	15.2–968.7	5.4	J1626–2951	J1517–2422	J1517–2422
	C43-1	2019 Jan 21	10.12	48	15.0–313.7	11.3	J1625–2527	J1517–2422	J1517–2422
	ACA	2018 Nov 18	34.83	10	8.9–44.7	30.3	J1625–2527	J1256–0547	J1256–0547
	ACA	2018 Nov 22	34.78	12	8.9–48.9	30.3	J1625–2527	J1337–1257	J1337–1257
Setup 2	C43-4	2018 Dec 1	20.73	43	15.1–951.7	5.3	J1625–2527	J1427–4206	J1427–4206
	C43-4	2019 Apr 17	20.75	46	15.1–740.4	5.6	J1650–2943	J1517–2422	J1517–2422
	C43-4	2019 Oct 11	20.72	43	15.1–783.5	5.5	J1626–2951	J1427–4206	J1427–4206
	C43-1	2019 Jan 21	7.10	48	15.0–313.7	10.0	J1625–2527	J1517–2422	J1517–2422
	ACA	2018 Oct 25	49.43	11	8.9–48.9	26.9	J1700–2610	J1924–2914	J1924–2914

Note.

^a Maximum recoverable scale.

flux calibration was 10% (R. Warmels et al. 2018). Images of C¹⁸O ($J = 2 - 1$), SO ($J_N = 6_5 - 5_4$), SO ($J_N = 6_6 - 5_5$), ³⁴SO ($J_N = 5_6 - 4_5$), CS ($J = 5 - 4$), SiO ($J = 5 - 4$), H¹³CO⁺ ($J = 3 - 2$), and DCO⁺ ($J = 3 - 2$) were obtained with the CLEAN algorithm of CASA (v.5.7.2-4) by employing Briggs weighting with a robustness parameter of 0.5. The beam size of the line emission is about 0^h5 × 0^h4 by combining the data with all of the antenna configurations (C43-4, C43-1, and ACA) as summarized in Table 1. The maximum recoverable scale⁵¹ of the observation with the ACA is 30^h3 according to the QA2 report. The images are corrected for the primary beam attenuation.

3. Results

3.1. Overall Morphology

Figure 1 shows the 1.2 mm continuum map of Elias 29. The continuum emission has its brightest peak at the protostar position. The continuum peak position is derived to be (α_{ICRS} ,

$\delta_{\text{ICRS}} = (16^{\text{h}}27^{\text{m}}09^{\text{s}}.41737 \pm 0^{\text{s}}.00007, -24^{\circ}37'19''.3104 \pm 0''.0007)$ with a peak flux density of 14.62 ± 0.06 mJy beam⁻¹ based on two-dimensional Gaussian fitting task `imfit` with CASA for the continuum image. The convolved and deconvolved sizes of the continuum emission are $(0''.550 \pm 0''.003) \times (0''.404 \pm 0''.001)$ and $(0''.165 \pm 0''.009) \times (0''.152 \pm 0''.005)$, respectively, where the synthesized beam size is $0''.52 \times 0''.37$ (PA = -70°). Other than this intensity peak, we found a weak north-south extension with a moderate emission peak of 0.63 mJy beam⁻¹ at 600 au southeast of the protostar, which belongs to the southern ridge component. Although this weak emission was not detected in Y. Oya et al. (2019), it was detected in this project likely thanks to both the higher sensitivity and the wider UV coverage from the inclusion of an ACA configuration. Scientific examination based on the continuum emission, including the 3 mm data taken as part of the FAUST program as well as the 1.2 mm data used here, will be reported separately.

Figure 2 shows the integrated and peak intensity maps of the SO ($J_N = 6_5 - 5_4$), CS ($J = 5 - 4$), and C¹⁸O ($J = 2 - 1$) lines. The southern ridge component is bright in all three species, while the continuum peak position is bright only in the SO emission. The distributions of SO and CS are confirmed to

⁵¹ See also Table 7.1 in ALMA Cycle 6 Technical Handbook (R. Warmels et al. 2018, <https://almascience.nao.ac.jp/documents-and-tools/cycle6/alma-technical-handbook#page=89>).

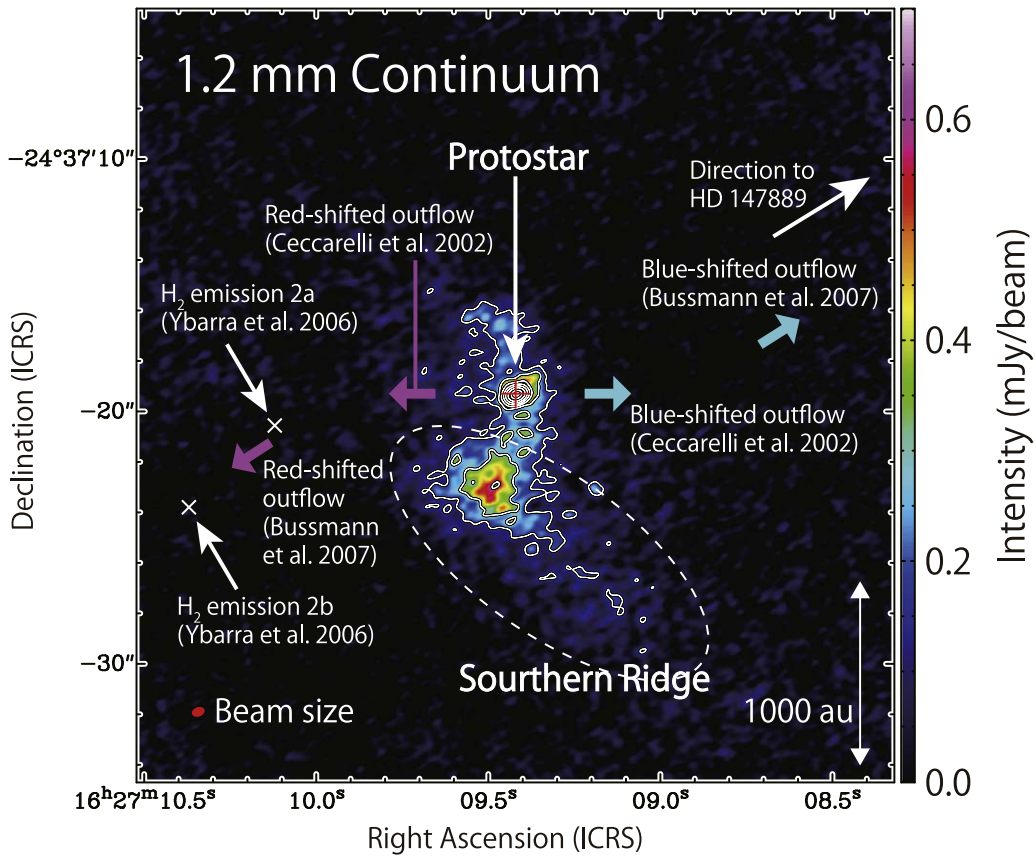


Figure 1. 1.2 mm continuum map. The red cross represents the continuum peak position at the location of the Elias 29 protostar, where the peak intensity is 15 mJy beam^{-1} . The southern ridge component is indicated by the white dashed ellipse. Contour levels are every two times starting from 5σ (i.e., 5σ , 10σ , 20σ , ...), where σ of $30 \mu\text{Jy beam}^{-1}$ is the rms noise level. The beam size is shown in the red ellipse at the bottom-left corner of the map. Magenta and cyan arrows represent the directions of the redshifted and blueshifted outflow lobes, respectively, previously reported by C. Ceccarelli et al. (2002) and R. S. Bussmann et al. (2007). White crosses represent the positions where the H_2 emission was reported by J. E. Ybarra et al. (2006). The white arrow on the northwestern side of the panel represents the direction to the B-type star HD 147889 taken from W. R. M. Rocha & S. Pilling (2018).

be consistent with that previously reported by Y. Oya et al. (2019) with a higher spatial resolution and sensitivity of our data. The distribution of C^{18}O is found to be extended over the field of view and is relatively weak at the continuum peak. The C^{18}O emission is generally more extended than the SO emission. Hence, the former can be more filtered out by the interferometer, although the maximum recoverable scale of $30''/3$ will contribute to recover the extended emission. Even if the C^{18}O emission were resolved out for the systemic velocity component due to contamination of the extended ambient component, the high velocity-shift components originating from the spin-up velocity structure near the protostar (L. Hartmann 2008; N. Ohashi et al. 2014; Y. Oya et al. 2022) should be detected as seen for the SO lines (Figure 3; see Section 3.2). In addition, a compact distribution should also be seen toward the protostar in the peak intensity map. A lack of these features (Figures 2(f) and 3) indicates that the C^{18}O emission is not resolved out significantly but is really weak around the protostar. The peak intensity map of the C^{18}O emission seems to have voids toward the northwest and southeast of the continuum peak position. This observed structure is likely related to the cavity produced by the outflow extending along the northwest–southeast direction (C. Ceccarelli et al. 2002; J. E. Ybarra et al. 2006; R. S. Bussmann et al. 2007), as discussed further in Section 4.1. We also note weak arc-like structures in the peak intensity map of the SO emission

(Figure 2(d)) with the intensity up to 51 mJy beam^{-1} detected by $\sim 5\sigma$, where σ of 10 mJy beam^{-1} is the rms noise level; the features on the eastern and western sides may trace the southeast and northwest outflow cavity walls, respectively (see also Section 4.1). Meanwhile, that on the southwestern side morphologically seems to be related to the southern ridge component.

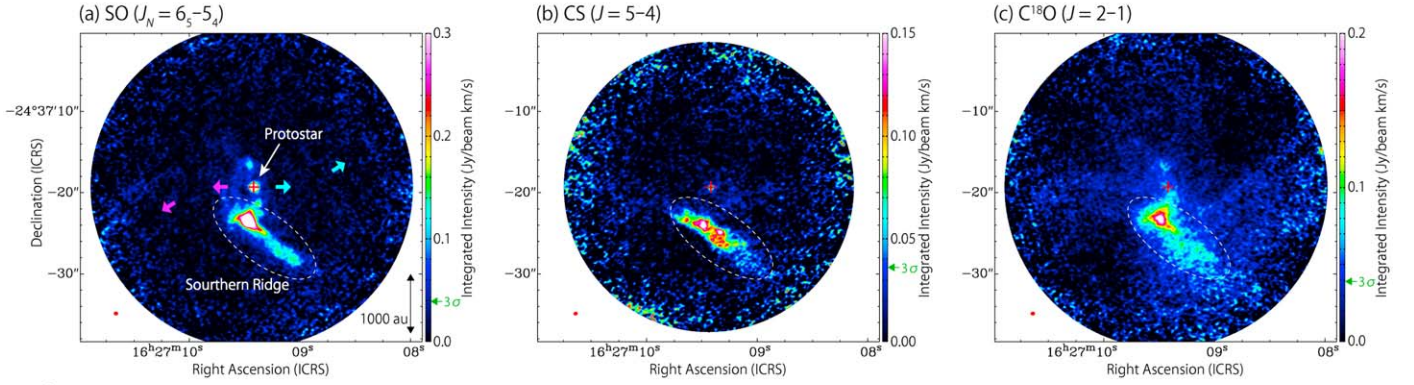
3.2. Temperature Distribution

In this Section, we investigate the distribution of the rotational temperature of SO by using its two observed transitions ($J_N = 6_5 - 5_4$, $E_{u1} = 35 \text{ K}$; $J_N = 6_6 - 5_5$, $E_{u2} = 57 \text{ K}$). Assuming the local thermodynamic equilibrium (LTE) and optically thin conditions, the rotational temperature (T_{rot}) of SO is derived from the ratio of the integrated intensities of its two lines according to the following equation:

$$\frac{W_2}{W_1} = \frac{\nu_1(S\mu^2)_2}{\nu_2(S\mu^2)_1} \exp\left(-\frac{E_{u2} - E_{u1}}{k_B T_{\text{rot}}}\right), \quad (1)$$

where W is the observed integrated intensity, ν is the frequency of the transition, S is the line strength, μ is the dipole moment responsible for the transition, and E_u is the upper-state energy. The ν , $S\mu^2$, and E_u values for each line are listed in Table 1,

Integrated Intensity Maps



Peak Intensity Maps

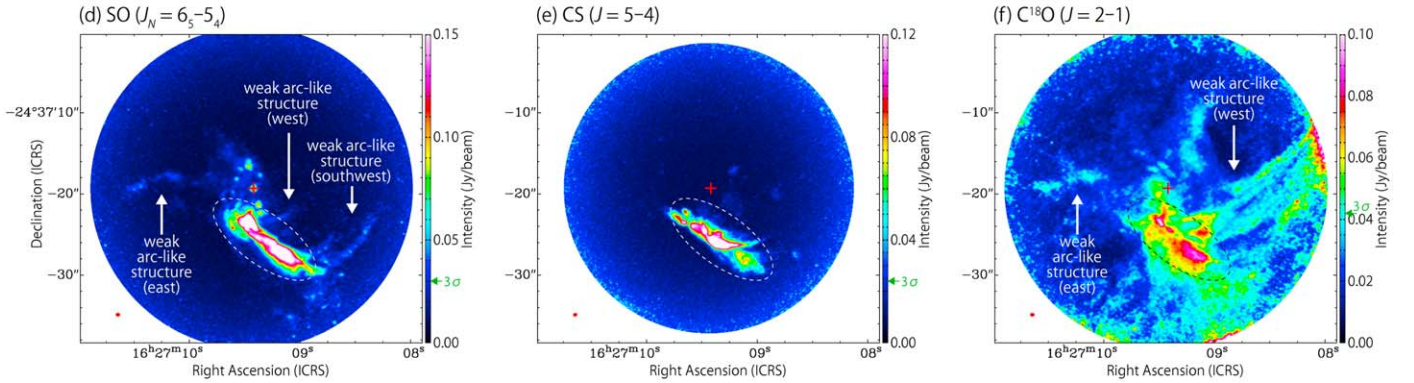


Figure 2. Panels (a), (b), and (c): integrated intensity (moment 0) maps of SO ($J_N = 6_5 - 5_4$), CS ($J = 5 - 4$), and $C^{18}O$ ($J = 2 - 1$), respectively. The velocity range for the integration is from -20 to 30 km s^{-1} . Panels (d), (e), and (f): peak intensity (moment 8) maps of the three molecular lines. The velocity range taken into account is from -20 to 30 km s^{-1} . The red cross in each panel represents the continuum peak position: $(\alpha_{\text{ICRS}}, \delta_{\text{ICRS}}) = (16^{\text{h}}27^{\text{m}}09^{\text{s}}.41737 \pm 0^{\text{h}}:00007, -24^{\circ}37'19''.3104 \pm 0''.0007)$. The red ellipse at the bottom-left corner in each panel represents the beam size for each molecular line. The magenta and cyan arrows in the top-left panel are the same as those in Figure 1. White and black dotted ellipses indicate the southern ridge component. The green arrow indicates the 3σ noise level in the color bar.

which are taken from CDMS (The Cologne Database for Molecular Spectroscopy; H. S. P. Müller et al. 2005; C. P. Endres et al. 2016). Suffixes 1 and 2, represent the $J_N = 6_5 - 5_4$ and $J_N = 6_6 - 5_5$ transitions, respectively. Figure 4(a) shows the map of the ratio of the integrated intensities of the two SO lines, and Figure 4(b) shows the map of the evaluated T_{rot} of SO.

The T_{rot} is mostly 20–30 K in the southern ridge component, except for a few small localized spots. We found three regions with a high rotational temperature in Figure 4(b); the component around the continuum peak position labeled as “C.P.,” the position at 500 au south of the protostar labeled as “position A” in the southern ridge component, and that at 500 au east of the protostar labeled as “position E.” Here, we specifically investigate the rotational temperature for these three positions and an additional three positions in the southern ridge (positions B, C, and D). The coordinates of these positions are summarized in Table 3. These positions are indicated in the maps in Figure 4. Positions A–D are taken to be aligned on the white line along the extension of the southern ridge component in Figure 4(a). Their central positions are separated by $2''$ from each other with the exception of the position between position A and position B, due to a complex velocity structure. Figure 3 shows the spectra of the SO lines observed at positions A–E and C.P.

The observed line parameters of SO for these positions are summarized in Table 4. Here, the spectra at positions A–D are averaged over a circular region with a diameter of $1''$ to increase the signal-to-noise ratio (S/N), while those at position E are taken at just 1 pixel to trace the compact structure of the bow-shocked region. The line profiles are generally asymmetric and deviate from the Gaussian shape (Figure 3). Thus, we do not employ the Gaussian fitting to derive the line parameters except for position E. For instance, the peak intensity of each line is evaluated from the peak value of the line profile (see the footnote of Table 4 for details).

From the integrated intensities of the two SO lines, the rotational temperature of SO at positions A–E and the continuum peak are derived by using Equation (1), as listed in Table 5. Since we use the integrated intensities in this analysis, the results do not suffer from the asymmetry of the line profile. We discuss a possible cause for the high temperature at positions A (53_{-15}^{+25} K) and E (72_{-29}^{+66} K) in Sections 4.1 and 4.2, respectively. Although there is also another candidate spot with a high rotational temperature (>60 K) on the southern side of “position C,” this result severely suffers from the error for the weak SO intensities; for instance, the rotational temperature is reduced to be 28 K by accounting for the 3σ error ($45 \text{ mJy beam}^{-1} \text{ km s}^{-1}$) of the SO ($J_N = 6_6 - 5_5$) line integrated intensity.

Since the evaluation of T_{rot} may suffer from the simple assumptions of the LTE and optically thin conditions, we

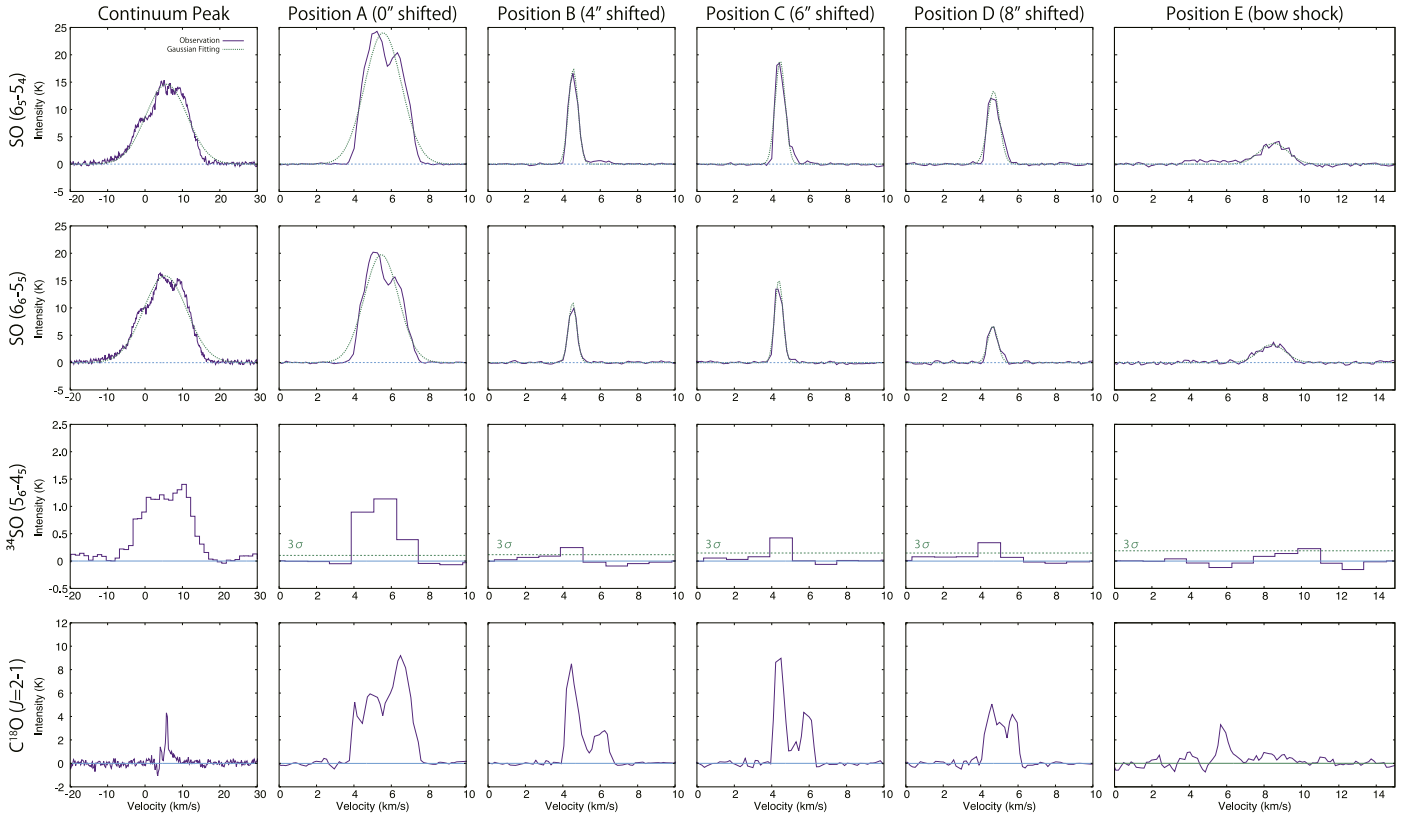


Figure 3. Spectra of the SO ($J_N = 6_5 - 5_4$, $J_N = 6_6 - 5_5$) and ^{34}SO ($J_N = 5_6 - 4_5$) lines at positions A–E (Figure 4). Coordinates of positions A–E are summarized in Table 3. Each spectrum is obtained as the average over the circular region with a diameter of $1''$ centered at each of positions A–D, while the spectrum at 1 pixel is employed for position E. A frequency resolution of ^{34}SO ($J_N = 5_6 - 4_5$) data is 1.129 MHz, while that of the other molecular line data is 141 kHz.

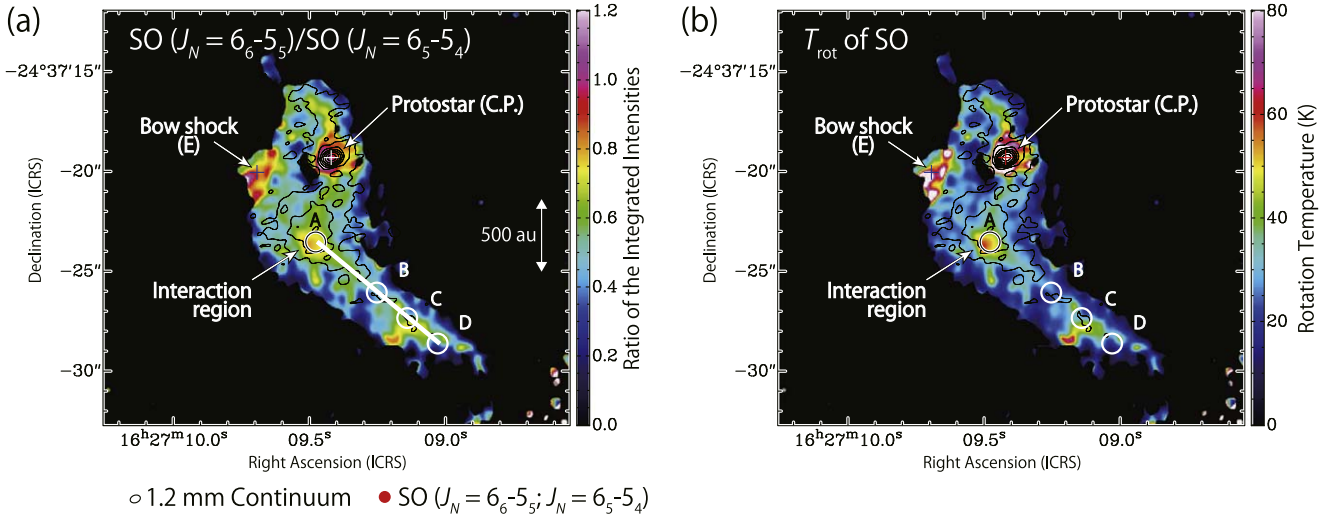


Figure 4. Maps of (a) the ratio of the integrated intensities of the two SO lines (b) and the rotational temperature of SO derived from the intensity ratio. The images of the two SO lines are smoothed so that their beam sizes are to be $0''.6 \times 0''.6$, as shown by the red circle outside the panels. The velocity range for the integration is from -15 to $+23$ km s^{-1} . Black contours in each panel represent the 1.2 mm continuum emission, where the contour levels are the same as those in Figure 1. The beam size of the continuum image is shown by a black ellipse outside the panels. (a) Ratio of the integrated intensity of the SO ($J_N = 6_6 - 5_5$) line to the SO ($J_N = 6_5 - 5_4$) line, which corresponds to W_2/W_1 in Equation (1). The pixels where the integrated intensity of the SO ($J_N = 6_5 - 5_4$) line is $< 2\sigma$ are shown in black, where σ of 18 mJy beam^{-1} is the rms noise level. (b) Rotational temperature of SO derived from the ratio of the integrated intensity of the two line emissions in panel (a). The pixels with negative values are shown in black, where the ratio of the integrated intensity is < 0 or higher than the high temperature limit (1.15 for $T_{\text{rot}} = \infty$). See the footnotes for Table 3 for the explanation about positions A–E.

confirmed its validity using a non-LTE analysis for positions A–E. We used the two SO lines data and one ^{34}SO line data to constrain the three free parameters (the gas kinetic temperature, the SO column density, and the H_2 number density) by the χ^2 method. We employed the photon-escaping probability for a

static, spherically symmetric, and homogeneous medium (D. E. Osterbrock & G. J. Ferland 2006; F. F. S. van der Tak et al. 2007). The spectra of the SO and ^{34}SO lines used for the non-LTE analysis are shown in Figure 3 for positions A–E, whose parameters are summarized in Table 4.

Table 3
Coordinates of Positions A–E and C.P

Position	R.A. (ICRS)	Decl. (ICRS)	Note
A	16 ^h 27 ^m 09 ^s .476	−24°37′ 23″.533	Outflow interaction in the southern ridge
B	16 ^h 27 ^m 09 ^s .251	−24°37′ 26″.104	4″ from position A along the southern ridge
C	16 ^h 27 ^m 09 ^s .139	−24°37′ 27″.390	6″ from position A along the southern ridge
D	16 ^h 27 ^m 09 ^s .027	−24°37′ 28″.675	8″ from position A along the southern ridge
E	16 ^h 27 ^m 09 ^s .692	−24°37′ 20″.043	Bow shock by the jet
C.P.	16 ^h 27 ^m 09 ^s .41737	−24°37′ 19″.3104	1.2 mm continuum peak position

Note. Spectra of the molecular lines are obtained as the averages over the circular region with a diameter of 1″ centered at each of positions A–D. Meanwhile, those with the original synthesized beam is employed for positions E and C.P.

Table 4
Parameters of the SO ($J_N = 6_5 - 5_4$, $J_N = 6_6 - 5_5$) and ^{34}SO ($J_N = 5_6 - 4_5$) Emissions

Position	Line	T_{peak}/K ^a	$V_{\text{LSR}}/\text{km s}^{-1\text{b}}$	$\Delta v/\text{km s}^{-1}$ ^c	$W/\text{K km s}^{-1\text{d}}$
A	SO ($J_N = 6_5 - 5_4$)	24.3(24)	5.24	2.32	56.6(57)
	SO ($J_N = 6_6 - 5_5$)	20.2(20)	5.02	2.15	43.4(43)
	^{34}SO ($J_N = 5_6 - 4_5$)	1.19(13)	2.67(13)
B	SO ($J_N = 6_5 - 5_4$)	16.57(17)	4.56	0.60	11.3(12)
	SO ($J_N = 6_6 - 5_5$)	9.92(99)	4.56	0.53	6.1(7)
	^{34}SO ($J_N = 5_6 - 4_5$)	0.48(58)	0.27(16)
C	SO ($J_N = 6_5 - 5_4$)	18.5(19)	4.42	0.64	12.9(14)
	SO ($J_N = 6_6 - 5_5$)	13.5(14)	4.33	0.53	7.9(9)
	^{34}SO ($J_N = 5_6 - 4_5$)	1.26(59)	0.73(17)
D	SO ($J_N = 6_5 - 5_4$)	12.0(12)	4.56	0.76	10.4(11)
	SO ($J_N = 6_6 - 5_5$)	6.53(65)	4.67	0.62	4.5(7)
	^{34}SO ($J_N = 5_6 - 4_5$)	0.83(65)	0.6(2)
E	SO ($J_N = 6_5 - 5_4$)	3.8(5)	8.50(8)	1.79(18)	6.1(7)
	SO ($J_N = 6_6 - 5_5$)	3.3(4)	8.42(6)	1.70(14)	5.2(6)
	^{34}SO ($J_N = 5_6 - 4_5$)	0.26(14)	10.0(5)	1.75(fixed)	0.4(2)
C.P.	SO ($J_N = 6_5 - 5_4$)	201(20)
	SO ($J_N = 6_6 - 5_5$)	230(23)
	^{34}SO ($J_N = 5_6 - 4_5$)	21(3)

Notes. The numbers in parentheses represent the error in units of the last significant digits.

^a Peak intensity of the observed line profiles for positions A–D. The error is evaluated from twice the rms noise of each spectrum and the 10% intensity calibration error, where the latter contribution dominates the total error. Since the ^{34}SO emission is frequency-diluted due to a coarse-resolution backend, its peak intensity is derived from the integrated intensity divided by the averaged line width of the two SO lines (see the [Appendix](#)). For position E, the peak intensity is derived by the Gaussian fitting.

^b LSR velocity of the intensity peak of the observed line profiles for positions A–D. For position E, the Gaussian fitted value is employed.

^c FWHM of the line width. The Gaussian fitted value is employed. Although the spectrum is not well fitted to define the peak intensity due to the asymmetric line shape for positions A–D, the line width obtained by the fit is approximately employed as the best effort.

^d Observed integrated intensity from 0.0 to +10.0 km s^{−1} for positions A–D, that from +7.0 to +10.5 km s^{−1} for position E, and that from −15.0 to +23.0 km s^{−1} for the continuum peak (C.P.) position.

Further details for the non-LTE analysis are described in the [Appendix](#).

4. Outflow/Jet Feedback as Candidate Causes for the Local Heating

4.1. Temperature Enhancement due to Outflow Interactions

In this Section, we discuss the region’s interaction with the outflow as the potential cause for the high temperature at position A. Figure 5 shows the velocity channel maps of the C¹⁸O and SO emissions. Although the overall structure is complex, we find a part of a parabolic feature extending over 20″ (~2700 au) oriented toward southeast from the protostar in

Figures 5(a), (b), and (d). We see a void of the C¹⁸O emission in its velocity channel map of +5.4 km s^{−1} (Figure 5(b)) inside the parabolic shape on the northwestern side of the protostar, while such a feature is not evident in the SO emission (Figure 5(e)). This feature is seen probably because the C¹⁸O emission traces the cavity wall of the northwestern outflow lobe.

The outflow of this source was previously reported based on the single-dish CO ($J = 6 - 5$) observation by C. Ceccarelli et al. (2002), where the outflow axis is extending along the east–west direction on 30″ scales. R. S. Bussmann et al. (2007) reported the inverse S-shaped structure of the outflow; the outflow axis is along the southeast–northwest direction on 100″

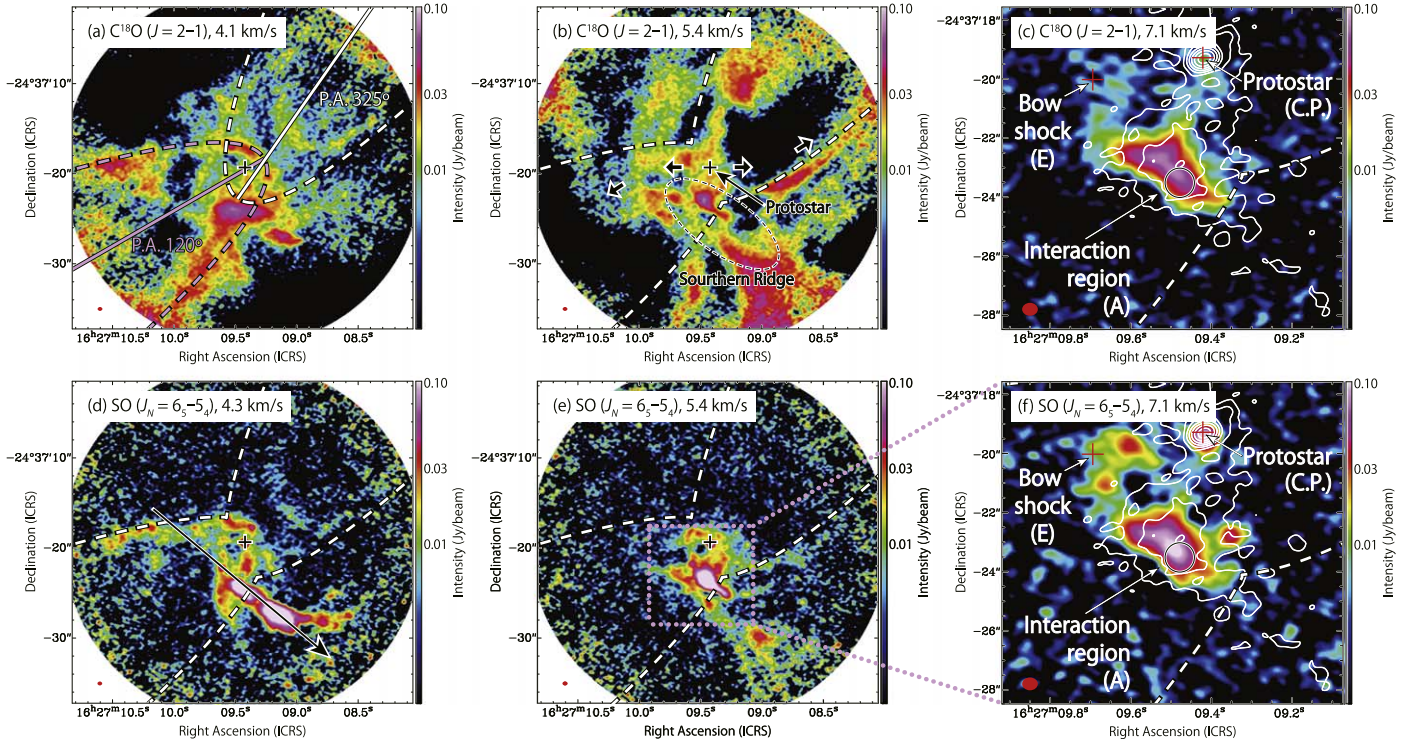


Figure 5. The velocity channel maps of the C^{18}O ($J = 2 - 1$; panels (a)–(c)) and SO ($J_N = 6_s - 5_s$; panels (d)–(f)) lines. Panels (a) and (d) show the velocity channel maps of the two molecular lines near the systemic velocity of the protostar ($\sim +4 \text{ km s}^{-1}$). Panels (b) and (e) show their velocity channel maps with the redshifted velocity (5.4 km s^{-1}). Panels (c) and (f) show the maps with a more redshifted velocity (7.1 km s^{-1}), focusing on the region around position A. The pink dotted rectangle in panel (e) indicates the region shown in panels (c) and (f). White contours in panels (c) and (f) represent the continuum emission, where the contour levels are the same as those in Figure 1. The beam size is depicted by a red ellipse at the bottom-left corner in each panel. Black or red crosses in each panel represent the protostellar position (C.P.). White and pink dashed lines indicate the outflow morphology obtained based on these panels. The central axes of the parabolic shapes are represented by white and pink solid lines in panel (a), which have position angles of 120° and 325° , respectively. The directions of the outflow lobes previously reported are indicated by the black arrows in panel (c), which are the same as the magenta and cyan arrows in Figure 1. The black arrow in panel (d) indicates the position axis along which Figure 6 is obtained.

Table 5
Column Density and Rotational Temperature of SO at Representative Positions

Position	LTE ^a		Non-LTE ^b		
	$N(\text{SO})/10^{14} \text{ cm}^{-2}$	T_{rot} (K)	$N(\text{SO})/10^{14} \text{ cm}^{-2}$	T_{kin} (K)	$n(\text{H}_2)/10^6 \text{ cm}^{-3}$
A	$8.4^{+1.2}_{-0.6}$	53^{+25}_{-13}	$10.7^{+1.2}_{-1.7}$	55^{+39}_{-14}	>1.2
B	$1.5^{+0.2}_{-0.2}$	28^{+7}_{-5}	$1.3^{+2.6}_{-0.2}$	>23	>0.2
C	$1.7^{+0.2}_{-0.1}$	34^{+10}_{-7}	$3.6^{+3.1}_{-1.6}$	26^{+15}_{-3}	>0.4
D	$1.5^{+0.3}_{-0.2}$	22^{+5}_{-4}	$7.3^{+11.0}_{-6.3}$	>16	>0.11
E	$1.0^{+0.5}_{-0.2}$	72^{+66}_{-29}	$1.2^{+0.8}_{-0.4}$	>56	>0.4
C.P.	>71	>192

Notes.

^a Values are derived under the assumptions of the LTE and optically thin conditions. See Sections 3.2 and 5.1. The observed integrated intensities are summarized in Table 4. The error is derived from the 2σ noise error in the integrated intensities and the intensity calibration error of 10%.

^b Values are derived by the non-LTE analyses. See the Appendix for the details. The observed peak intensities are summarized in Table 4. The error is derived from the 2σ noise error in the intensities and the intensity calibration error of 10%.

scales, while it is tilted to be along the south–north direction on larger scales. These outflow directions are consistent with the shocked knots seen in the H_2 infrared emission-line image reported by J. E. Ybarra et al. (2006). Considering these previous reports, the parabolic and void features found in Figure 5 likely represent the outflow cavities.

To explore the outflow–ridge interaction feature at position A, we produced a position–velocity (PV) diagram of the SO emission along the southern ridge (Figure 6). The position axis

of the PV diagram is taken to pass through the crossing point of the outflow cavity and the southern ridge, as shown in Figure 5(d). The spatially extended component traces the southern ridge at the systemic velocity of $\sim +4.5 \text{ km s}^{-1}$. Moreover, a bright component is locally seen at position A with velocity ranging from $+4.5 \text{ km s}^{-1}$ to $+7 \text{ km s}^{-1}$, which is redshifted by $0\text{--}2.5 \text{ km s}^{-1}$ from the systemic velocity of the southern ridge ($\sim +4.5 \text{ km s}^{-1}$) and by $0.5\text{--}3 \text{ km s}^{-1}$ from that of the protostar ($+4 \text{ km s}^{-1}$). This strong localized emission

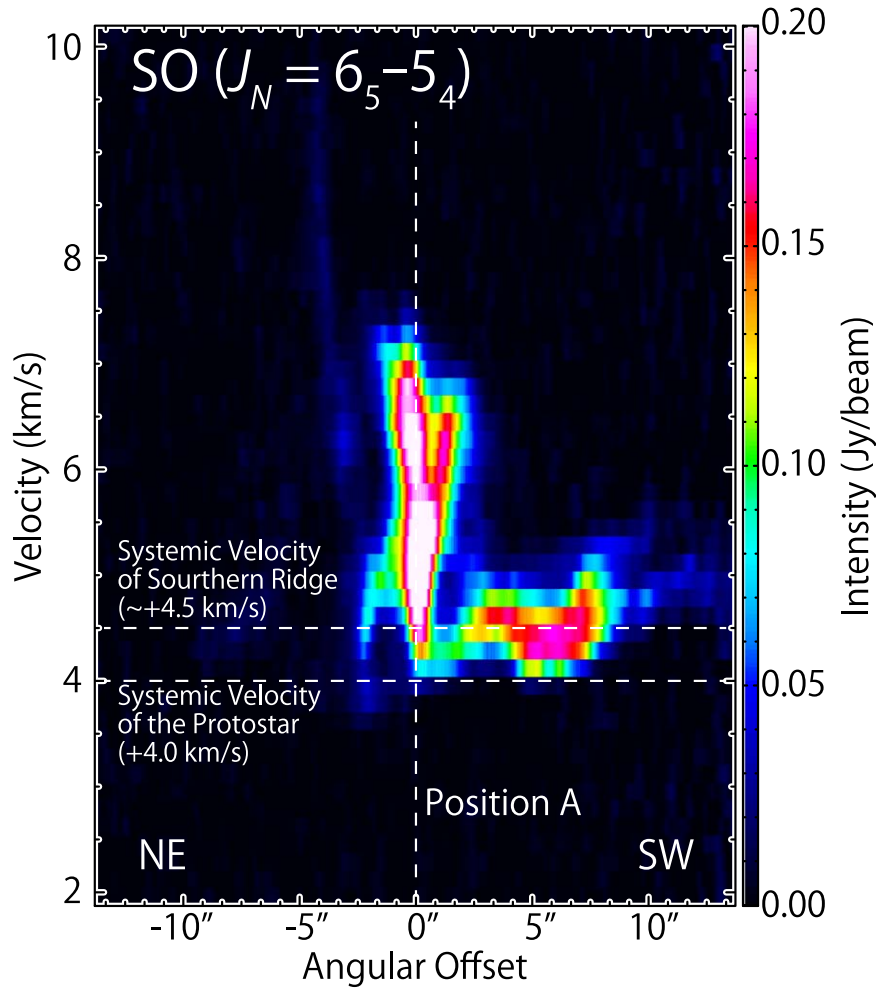


Figure 6. Position–Velocity diagram of the SO ($J_N = 6_5 - 5_4$) line. The position axis is taken along the southern ridge component as shown by the black arrow in Figure 5(d). Angular offset of $0''$ shown by the dashed vertical line is taken at position A. The dashed horizontal lines represent the systemic velocity of the southern ridge ($+4.5 \text{ km s}^{-1}$) and that of the protostar ($+4.0 \text{ km s}^{-1}$).

can be confirmed in the velocity channel maps of $+5.4$ and $+7.1 \text{ km s}^{-1}$ for both the C^{18}O and SO emissions (Figures 5(b), (c), (e) and (f)). The redshifted feature is consistent with the previous reports for the eastern outflow lobe by C. Ceccarelli et al. (2002) or the southeastern one by R. S. Bussmann et al. (2007). Among the spectra of the ^{12}CO ($J = 6 - 5$) reported by C. Ceccarelli et al. (2002; see their Figure 1), the spectrum at $7''$ south of the protostar is the one obtained at the position nearest to position A. The ^{12}CO emission peaks at $+6 \text{ km s}^{-1}$ and shows a wing there, which was interpreted to trace the outflowing gas (C. Ceccarelli et al. 2002). This ^{12}CO feature, therefore, seems to correspond to the redshifted component of the SO emission in our Figure 6. Hence, the SO emission at position A is naturally interpreted as kinematic evidence of the interaction of the outflow with the southern ridge.

Since position A is located within the north–south extension of the dust continuum emission (see Figures 1 and 4), one may contemplate whether the warming is due to an additional protostar, perhaps with the larger southern ridge supplying mass. The distribution of the continuum emission around this local peak, however, is broad and not localized, in contrast to that toward the known protostar of Elias 29. Furthermore, the SO emission does not show a clear velocity gradient, expected if gravity is playing a role (e.g., Y. Oya et al. 2022). While the

Two Micron All Sky Survey Bands H and J data shows an intensity peak at the protostellar position of Elias 29, we do not find any peaks centered at position A indicating a pointlike young stellar object candidate by using Aladin Sky Atlas (F. Bonnarel et al. 2000). Although we cannot rule out the protostar solution completely, the evidence provides stronger support to a shocked region. In this case, the dust continuum emission has been enhanced due to both an increased density and temperature from the shock; such a feature was reported for a young low-mass protostellar source IRAS 16293–2422 by M. J. Maureira et al. (2022).

4.2. Temperature Enhancements due to Jet Shock Interactions

The other clear hot spot, position E, is on the eastern side of the protostar. It is located inside the southeastern outflow cavity structure, whose central axis has a position angle (P.A.) of $\sim 120^\circ$, seen in the C^{18}O emission (Figure 7(a)). Furthermore, it is nearly on the central axis of the parabolic shape of the outflow morphology represented by the pink solid line in Figure 7(a), which likely corresponds to the outflow axis. The emission at position E is evident in the velocity channel map of $+8.3 \text{ km s}^{-1}$ as shown in Figure 7(a). This emission is redshifted by $+4.3 \text{ km s}^{-1}$ with respect to the systemic velocity of the protostar ($\sim +4 \text{ km s}^{-1}$). This observed velocity shift

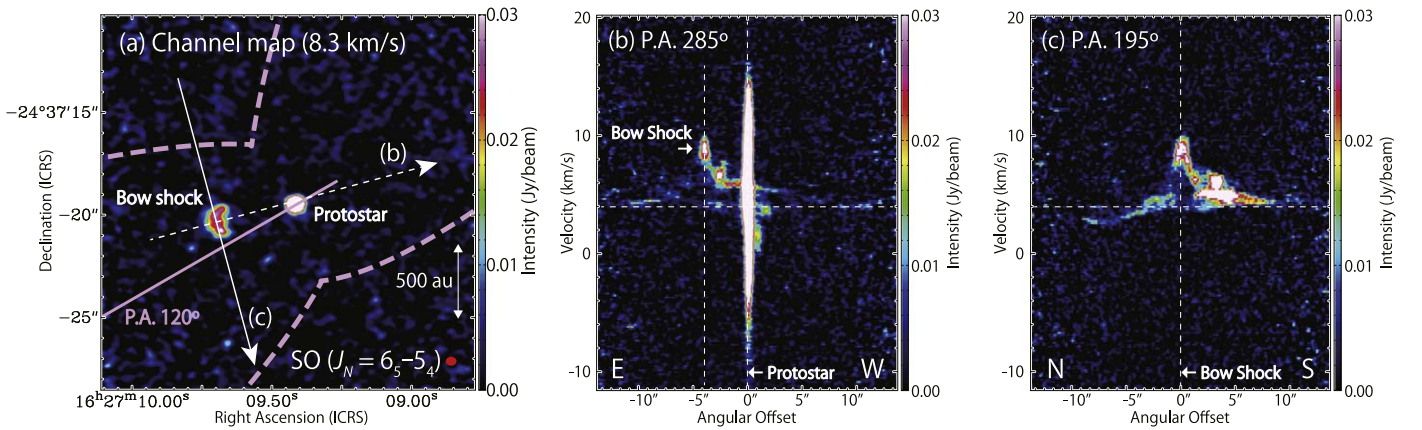


Figure 7. Panel (a): velocity channel map of the SO ($J_N = 6_5 - 5_4$) line. Velocity of $+8.3 \text{ km s}^{-1}$ is redshifted from the systemic velocity of the protostar ($\sim +4 \text{ km s}^{-1}$). The pink dashed and solid lines are the same as those in Figure 5. Panels (b) and (c): position–velocity diagrams of the SO ($J_N = 6_5 - 5_4$) line. Position axes for panels (b) and (c) are shown by the white dashed and solid arrow in panel (a), respectively. White vertical lines in panels (b) and (c) represent the protostellar position and position E, respectively. White horizontal lines in panels (b) and (c) represent the systemic velocity of the protostar ($+4.0 \text{ km s}^{-1}$).

along the line of sight corresponds to a propagating velocity of 24.8 km s^{-1} after correcting for projection using the inclination angle of 80° reported by Y. Oya et al. (2019). The direction from this position to the protostar (P.A. 285°) roughly corresponds to the direction of the outflow cavity structure (P.A. 120°) discussed in Section 4.1. Thus, one possible cause for this feature is a bow shock produced by the interaction between the protostellar jet and the ambient gas, which has remained undissipated by the outflow.

To verify this picture, we obtained PV diagrams around position E, as shown in Figures 7(b) and (c). The position axes are passing through position E (Figure 7(a)). Figure 7(b) shows the PV diagram obtained through position E and the protostellar position. The compact component concentrated to the protostar is seen as the bright emission with a wide velocity range from -8 to $+16 \text{ km s}^{-1}$ at the angular offset of $0''$. This disk/envelope component was previously analyzed by Y. Oya et al. (2019). In addition to the compact feature, we see several bright knots east of the protostar. The knot with velocity from $+8$ to $+10 \text{ km s}^{-1}$ corresponds to the emission at position E. Taken together, these knots show a velocity gradient from the protostar to position E; they seem to be accelerated from the systemic velocity of $+4 \text{ km s}^{-1}$ at the protostar. Figure 7(c) shows the PV diagram across the outflow lobe passing through position E. In addition to the widely extended ($\sim 20''$) and slow (from $+2$ to $+6 \text{ km s}^{-1}$) component of the outflow structure, we find bright emission associated with a localized ($< 2''$) and fast (from $+8$ to $+10 \text{ km s}^{-1}$) component. This behavior is naturally expected for a bow shock (e.g., M. Gustafsson et al. 2010); a bow shock presents the maximum acceleration of the gas at its apex, while the shocked gas is less perturbed away from the axis of the shock. Thus, the bright emission at position E is interpreted to be a bow shock produced by the narrow jet from the protostar.

It is worth noting that a feature morphologically similar to what we found in Figure 7(b) was found in the SiO emission toward IRDC (infrared dark cloud) G034.77–00.55 (Figure 4 by G. Cosentino et al. 2019) caused by an interaction with the supernova remnant W44, which was interpreted to be a magnetohydrodynamic C-shock. While the shock in G034.77–00.55 was suggested to be produced by the deceleration due to the dense material of the IRDC, the shocked gas in Elias 29

seems to accelerate. Thus, we need the shock modeling to examine whether the observed feature is related to a C-shock.

Assuming that the typical observed velocity of the bow shock ($+8 \text{ km s}^{-1}$; Figure 7) is comparable to the propagating velocity projected onto the plane of the sky and that the systemic velocity is $+4 \text{ km s}^{-1}$, the dynamical timescale of the bow shock is roughly estimated to be

$$t_{\text{dyn}} = \frac{d_{\text{shock}}}{v_{\text{jet}}} \sim \frac{600}{\tan(i)} \text{ yr.} \quad (2)$$

Here, d_{shock} denotes the deprojected distance from the protostar to the bow shock, v_{jet} is the deprojected propagating velocity of the jet, and i is the inclination angle of the jet axis with respect to the line of sight, where an i of 0° corresponds to the pole-on geometry. For instance, t_{dyn} , d_{shock} , and v_{jet} are obtained to be 110 yr, 560 au, and 23 km s^{-1} , respectively. Y. Oya et al. (2019) reported a lower limit of 65° for i based on the ellipticity of the continuum emission, and Y. Oya et al. (2022) reported that the rotation motion of the gas associated to the protostar is well reproduced by the Keplerian motion with an i of 80° . Then, we assume an i of 80° in the above calculation. If we employ the lower (65°) and upper limit (120°) for i discussed in the above literature, t_{dyn} is calculated to be 280 yr and 350 yr, respectively. If this short timescale of the shock is the case, this would suggest that a mass accretion onto the protostar still occurs in this late Class I source.

4.3. Mass Accretion in the Disk/Envelope System

As described in Sections 4.1 and 4.2, we found a young and energetic outflow/jet emerging from the protostar in this study. This result suggests that significant mass accretion is continuing at least sporadically. Although Elias 29 is a protostellar source at a late Class I stage, Y. Oya et al. (2022) reported that there is still a hint of infall motion of the gas in the compact structure in the vicinity of the protostar in addition to the Keplerian motion.

The relatively large bolometric luminosity ($L_{\text{bol}} = 13.6 L_\odot$; D. Lommen et al. 2008; A. Miotello et al. 2014) also suggests a moderate accretion rate. When we employ the protostellar mass (M) of $0.8 M_\odot$ (Y. Oya et al. 2022), the mass accretion rate (\dot{M}) is roughly evaluated to be $1.4 \times 10^{-6} M_\odot \text{ yr}^{-1}$ by using the

following equation given by F. Palla & S. W. Stahler (1991):

$$\dot{M} = \frac{L_{\text{bol}} R}{GM}, \quad (3)$$

where G denotes the gravitational constant. Here, we assume a protostar radius (R) 2.5 times the solar radius (R. B. Larson 2003). This mass accretion rate is comparable to the typical value during the main accretion phase (e.g., L. Hartmann 2008) and, thus, is larger than that expected at the end of the Class I stage. Such a high accretion rate ($>10^{-6} M_{\odot} \text{ yr}^{-1}$) was also reported for a considerable number of Class I sources by M. L. Enoch et al. (2009; see Figure 12 in their paper). These authors concluded that the mass accretion during the Class I stage is episodic, considering the large dispersion in the observed bolometric luminosity.

The disk mass derived from the continuum emission is reported to be $(7.3 \pm 0.6) \times 10^{-3} M_{\odot}$ (E. Artur de la Villarmois et al. 2019). Hence, the disk lifetime should be of the order of 10^{3-4} yr, if the accretion from the disk component toward the protostar is continuous at the rate evaluated above. This source does not have a massive surrounding envelope that could sustain a continuous accretion at the above rate, as revealed by the lack of such components in our C^{18}O and CS data. With these considerations, the outflow/jet activities are expected to be sporadic rather than continuous, and the protostar would currently be in a relatively high accretion phase that could not last for a long time.

The indication of stronger accretion than expected for a late Class I source and the observation of a bow-shaped shock along the jet, within the southeast outflow lobe, suggests that Elias 29 should be investigated for potential accretion variability, as suggested for another luminous Class I source in Perseus by M. T. Valdivia-Mena et al. (2022). Unsteady mass assembly during the protostar stage is expected and observed, and can be an important probe of the underlying physical conditions in the disk (W. J. Fischer et al. 2023). The JCMT (James Clerk Maxwell Telescope) Transient Survey (G. J. Herczeg et al. 2017) has been monitoring Ophiuchus, including Elias 29, for over 8 yr (Y.-H. Lee et al. 2021; S. Mairs et al. 2024) at $850 \mu\text{m}$ with a $15''$ beam and thus far has found no evidence of variability for this source. The same survey, however, has shown that at least 25% of protostars are variable on years-long timescales, with these sources showing both episodic variations (e.g., EC 53; Y.-H. Lee et al. 2020) and burst behavior (e.g., HOPS 373; S.-Y. Yoon et al. 2022). Therefore, continued monitoring of Elias 29 is strongly encouraged.

5. Chemical Characteristics in the Shocked and Warm Environment

5.1. Column Density of SO at the Shock Locations

We evaluated the column density of SO ($N(\text{SO})$) for the six positions shown in Figure 4 under the assumption of the LTE condition with T_{rot} derived in Section 3.2 by using the following equation:

$$N(\text{SO}) = U(T_{\text{rot}}) \frac{3k_{\text{B}} W}{8\pi^3 \nu S \mu^2} \exp\left(\frac{E_{\text{u}}}{k_{\text{B}} T_{\text{rot}}}\right), \quad (4)$$

where $U(T_{\text{rot}})$ denotes the partition function of SO at the temperature T_{rot} , and k_{B} is the Boltzmann constant. The line

parameters (the frequency ν , $S\mu^2$, and E_{u}) are summarized in Table 1, while the integrated intensities are in Table 4. Since the integrated intensity W is used, the derived column density is an averaged one over velocity components along the line of sight. The results of the LTE analysis are summarized in Table 5. The obtained column density of SO is similar to each other among positions B–E ($(1.0\text{--}1.7) \times 10^{14} \text{ cm}^{-2}$) while it is about 5 times higher at position A ($8.4 \times 10^{14} \text{ cm}^{-2}$). Only the lower limit was obtained at the continuum peak position due to the high opacity of the SO lines. We also conducted a non-LTE analysis for confirmation in the Appendix and found that the column densities derived under the LTE assumption are almost consistent with those derived by the non-LTE analysis, except for position D with a large error; the difference of the evaluated values are within 20% for positions A, B, and E between the two analyses, while the evaluated values are different by a factor of 2 for position C. The error for the non-LTE result is large because the H_2 density is treated as a free parameter as well as the gas kinetic temperature and the column density (see the Appendix).

In principle, it is desirable to derive the SO abundance relative to H_2 by using the H_2 estimated from the C^{18}O data. However, the line profiles of C^{18}O at positions A–E are different from those of SO (Figure 3). The C^{18}O line has a lower critical density than the SO lines and would preferentially trace different parts along the line of sight. Thus, it is almost impossible to disentangle these components and derive their SO abundances reasonably. Hence, we just discuss the SO column densities in this paper.

SO is often recognized as a shock tracer (e.g., R. Bachiller & M. Pérez Gutiérrez 1997); its abundance in the gas phase is expected to be increased by the sputtering of S atoms and/or SO from dust or ice mantle in shocked regions. The SO column density at the outflow interaction region (position A) is indeed higher than those at other positions in the southern ridge (positions B–D), which would indicate a sign of shock enhancement. However, the SiO ($J = 5 - 4$) line is undetected toward position A in our observation, although the SiO emission has been detected and associated with jets and strong shocks in other sources (e.g., H. Mikami et al. 1992; R. Bachiller & M. Pérez Gutiérrez 1997; L. A. Zapata et al. 2009; S. Feng et al. 2016; Y. Oya et al. 2018b, 2018a; Y. Okoda et al. 2021; A. Sato et al. 2023) due to the destruction and sputtering of silicate dust grains (L. M. Ziurys et al. 1989; P. Caselli et al. 1997; P. Schilke et al. 1997). Therefore, the shock at position A may not be strong enough to destroy or sputter dust grains to liberate SiO into the gas phase. The high column density of SO at position A may alternatively be due to the high gas column density at that location. In this case, the SO molecules are not originating from dust/ice mantle, but are already in the gas phase prior to the shock.

For position E, the SO column density is comparable to the quiescent parts of the southern ridge (positions B–D). Moreover, a lack of SiO emission at position E is puzzling, considering that the bow shock feature is observed. A detailed relation of position E to the outflow is not fully understood and might need further investigation both in observations and modeling.

Y. Oya et al. (2019) previously suggested that the warm environment of Elias 29 prevents C atoms and CO molecules from being adsorbed onto dust grains in the envelope such that

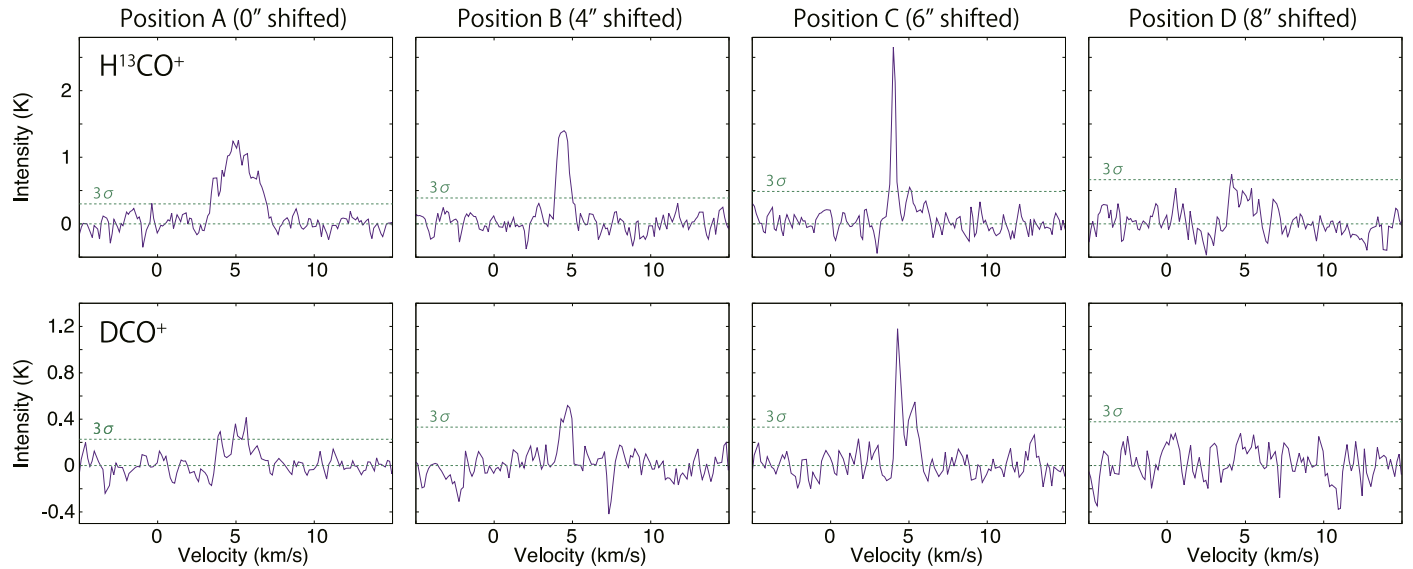


Figure 8. Spectra of the H^{13}CO^+ ($J = 3 - 2$) and DCO^+ ($J = 3 - 2$) lines. The spectra are obtained for positions A–D (Figure 4). Coordinates of positions A–D are summarized in Table 3. Each spectrum represents the average over the circular region with a diameter of $1''$ centered at each of positions A–D.

Table 6
Parameters of the H^{13}CO^+ and DCO^+ Spectra in the Southern Ridge

Position	Line	$T_{\text{peak}}/\text{K}^{\text{a}}$	$V_{\text{LSR}}/\text{km s}^{-1\text{b}}$	$\Delta v/\text{km s}^{-1\text{c}}$
A	H^{13}CO^+ ($J = 3 - 2$)	1.15(14)	5.14(8)	2.46(20)
	DCO^+ ($J = 3 - 2$)	0.29(7)	5.3(2)	1.9(5)
B	H^{13}CO^+ ($J = 3 - 2$)	1.56(22)	4.41(4)	0.84(10)
	DCO^+ ($J = 3 - 2$)	0.56(17)	4.60(10)	0.77(24)
C	H^{13}CO^+ ($J = 3 - 2$)	2.7(5)	4.03(2)	0.31(6)
	DCO^+ ($J = 3 - 2$)	1.2(4)	4.31(8)	0.37(20)
D	H^{13}CO^+ ($J = 3 - 2$)	0.51(19)	4.7(2)	1.6(6)
	DCO^+ ($J = 3 - 2$)	$<0.20^{\text{d}}$

Notes. The numbers in parentheses represent the error in units of the last significant digits, which is derived from the 2σ noise error and the intensity calibration error of 10%.

^a Peak intensity derived by the Gaussian fitting for each spectrum.

^b LSR velocity at the intensity peak derived by the Gaussian fitting for each spectrum.

^c FWHM of the line width derived by the Gaussian fitting for each spectrum.

^d Since the DCO^+ emission is too weak to perform the Gaussian fitting at position D, we employ the 2σ value as the upper limit for T_{peak} .

this source is deficient in organic molecules. If this is also the case for S atoms, the majority of SO molecules would need to be formed and preserved in the gas phase. This is likely the case because the desorption temperature of S atoms (1100 K) is less than or comparable to that of C atoms (800 K) and CO molecules (1150 K) according to Kinetic Database for Astrochemist (V. Wakelam et al. 2012; <http://kida.obs.u-bordeaux1.fr/>), as discussed by Y. Oya et al. (2019).

5.2. Deuterium Fractionation Ratio in the Southern Ridge

The line width of the SO emission is $<1 \text{ km s}^{-1}$ at positions B–D, as shown in Table 4 and Figures 3 and 6. Hence, it is difficult to explain the moderately high rotational temperature of SO (20–30 K; Table 5) at these three positions in terms of the recent outflow shock. This situation is different from that at positions A and E with larger line width, where interactions with the outflow/jet are seen in the velocity structure as discussed in Sections 4.1 and 4.2. Thus, it is important to assess

these derived moderately high temperatures in an independent way.

As an indicator for the temperature environment, we investigate the deuterium fractionation ratio of HCO^+ in the southern ridge component. For this purpose, we use the H^{13}CO^+ ($J = 3 - 2$) and DCO^+ ($J = 3 - 2$) emission, assuming the constant $[\text{HCO}^+]/[\text{H}^{13}\text{CO}^+]$ ratio of 60 (R. Lucas & H. Liszt 1998). The spectra of H^{13}CO^+ and DCO^+ emission toward positions A – D are shown in Figure 8, and the line parameters are summarized in Table 6. The observed peak intensity of the DCO^+ spectrum is lower than the noise level at position D, and thus, the 2σ noise error is employed as the upper limit. We employ a non-LTE analysis for both of the molecular lines, as we performed for the SO lines (see the Appendix for the details). H_2 is assumed to be the collision partner. Since the collisional cross sections of H^{13}CO^+ are not available, we employ those of HCO^+ for H^{13}CO^+ . The collisional cross sections of HCO^+ and DCO^+ are taken from Leiden Atomic and Molecular Database (F. L. Schöier et al. 2005), the original data of which were

Table 7
Deuterium Fractionation Ratio in the Southern Ridge

Position	$N(\text{H}^{13}\text{CO}^+)/10^{11} \text{ cm}^{-2}$	$N(\text{DCO}^+)/N(\text{H}^{13}\text{CO}^+)$	$N(\text{DCO}^+)/N(\text{HCO}^+)$
A	12_{-3}^{+11}	$0.3_{-0.1}^{+0.2}$	$0.005_{-0.002}^{+0.003}$
B	7_{-2}^{+25}	$0.4_{-0.3}^{+0.2}$	$0.007_{-0.005}^{+0.003}$
C	5_{-1}^{+10}	$0.5_{-0.4}^{+0.3}$	$0.009_{-0.006}^{+0.005}$
D	6_{-3}^{+37}	<0.94	<0.015

Notes. The temperature and density ranges are assumed to be equal to that derived from the non-LTE analysis of the SO lines (Table 5).

reported by O. Denis-Alpizar et al. (2020). For HCO^+ , the collisional cross sections with para- H_2 and ortho- H_2 are separately listed. We assume the ortho-para ratio of H_2 to be 3 in the analysis. Note that the following results do not change significantly by using an ortho-to-para ratio of 0.

In the χ^2 analysis, we use the peak intensities of the H^{13}CO^+ and DCO^+ intensities listed in Table 6. The χ^2 values for H^{13}CO^+ and DCO^+ were summed up to obtain the total χ^2 value, which is used to constrain the ranges of the H^{13}CO^+ column density and the $[\text{DCO}^+]/[\text{H}^{13}\text{CO}^+]$ ratio. In this analysis, the ranges of the gas kinetic temperature and the H_2 number density are assumed to be those derived in the non-LTE analysis for the SO emission (Tables 5).

The estimated $[\text{DCO}^+]/[\text{HCO}^+]$ ratio is summarized in Table 7. The $[\text{DCO}^+]/[\text{HCO}^+]$ ratio is below 1.5% including the error for all of the positions. These values are relatively low in comparison with those found in typical cold prestellar cores ($\sim 4\%$; A. Bacmann et al. 2003). This result indicates a relatively warm condition for the entire southern ridge. This is consistent with the result for the rotational temperature and the gas kinetic temperature derived for SO (Section 3.2).

It is interesting that a moderately high temperature is found even in the quiescent part of the southern ridge. One possible cause for this result is the external illumination by HD 147889, a B-type star at $700''$ (~ 0.5 pc) northwest of Elias 29. This star is suggested to heat the entire area, and even the whole Ophiuchus molecular cloud. Indeed, W. R. M. Rocha & S. Pilling (2018) reported that the molecular cloud core of Elias 29 is warmed up to more than 20 K by HD 147889 based on their radiative transfer modeling.

The relatively warm conditions in the southwestern part of the southern ridge without apparent influence of the ongoing outflow interaction may also explain the lack of iCOMs and hydrocarbon molecules in Elias 29. If the gas temperature of the parent cloud of Elias 29 was higher than 20 K due to the irradiation from HD 147889, CO molecules and C atoms would not deplete onto dust grains in the prestellar core phase. As a result, iCOMs and CH_4 are not produced efficiently via dust surface reactions (Y. Oya 2022). This possibility was pointed out by Y. Oya et al. (2019), and it is further strengthened by the temperature structure revealed in this project. Elias 29 is a novel example where the combination of environmental dynamics and radiation triggers peculiar chemistry. This situation is possibly similar to that of the photodissociation region (PDR) R CrA IRS7B (Y. Watanabe et al. 2012; J. E. Lindberg et al. 2015) where the abundance of iCOMs has been found to be unexpectedly deficient in a single-dish survey. On the other hand, the difference is the abundance of the CCH emission, which is known to be enhanced by the PDR (photodissociation region). The fractional abundance of CCH to H_2 is reported to be $(5.3 \pm 1.5) \times 10^{-9}$ in R CrA IRS7B with the gas temperature assumed to be 20 K

(Y. Watanabe et al. 2012), while its upper limit is $(1.3\text{--}9.0) \times 10^{-11}$ in Elias 29 with the gas and dust temperatures assumed to be from 50–150 K (Y. Oya et al. 2019). This large difference in the fractional abundance of CCH by 2 orders of magnitude implies that the PDR chemistry is not working in Elias 29, probably due to heavier attenuation of the far-UV photons dissociating CO.

6. Summary

In order to characterize the protostellar activity of the late Class I source Elias 29, we observed lines of SO, ^{34}SO , C^{18}O , CS, SiO, H^{13}CO^+ , and DCO^+ at a spatial resolution of 70 au ($0''.5$). This investigation is part of the ALMA large program FAUST. Our major findings are summarized below:

- (1) We delineated the temperature distribution by using two transitions of SO and one of ^{34}SO . We obtained a two-dimensional map of the rotational temperature of SO, using LTE assumptions, and found two hot spots with a rotational temperature of 53_{-15}^{+25} and 72_{-29}^{+66} K in addition to the hot component associated with the protostar. These locally high temperatures were confirmed with a non-LTE analysis.
- (2) The local increase of the temperature at the northeastern tip of the southern ridge component is likely attributed to interaction with the southeast outflow lobe. The other local temperature increase is interpreted as the result of a bow shock produced by the jet. It is interesting that Elias 29 still has significant outflow/jet activity at least sporadically in spite of its classification as a late-type Class I.
- (3) It is likely that significant mass accretion from disk to protostar is still occurring at least sporadically, considering the energetic activity of the outflow/jet in Elias 29 observed in this project, the hint of the infall motion in its disk/envelope system previously suggested, and its relatively large luminosity. The mass accretion rate is roughly evaluated to be $1.4 \times 10^{-6} M_{\odot} \text{ yr}^{-1}$, which sounds high for the late Class I stage of this source. Since the outer envelope has already been consumed/dissipated, as demonstrated by the lack of the C^{18}O emission associated around the protostar, we are likely witnessing the near end of the mass accretion phase.
- (4) We evaluated the SO column density at five positions (positions A–E). Although the SO column density at the outflow-ridge interaction region (position A) is found to be higher by a factor of 5 than in the quiescent part of the southern ridge (positions B–D), the SiO emission is not detected there. This result may indicate that the shock is not strong enough to destruct or sputter the silicate dust grains at position A. In spite of the bow-shock feature at position E, the SiO emission is not detected there either,

and the SO column density is comparable to those at positions B–D. The origin of these results at position E is still puzzling; further observational and modeling efforts are necessary.

- (5) Even the quiescent parts of the southern ridge at distances ranging from 500–1000 au away from the protostar are found to be moderately warm (20–30 K). This warm condition is consistent with our estimated relatively low deuterium fractionation (1% or less) in HCO^+ . The B-type star HD 147889, which is $700''$ away from Elias 29, would likely have kept the parent cloud of Elias 29 warm. Such a warm environment for the entire lifetime of this source could be the cause for its peculiar chemical characteristics including a deficiency of iCOMs and hydrocarbon molecules.

Acknowledgments

This paper makes use of the following ALMA data: ADS/JAO.2018.1.01205.L. ALMA is a partnership of ESO (representing its member states), NSF (USA), and NINS (Japan), together with NRC (Canada), NSC and ASIAA (Taiwan), and KASI (Republic of Korea), in cooperation with the Republic of Chile. The Joint ALMA Observatory is operated by ESO, AUI/NRAO, and NAOJ. This study is supported by Grant-in-Aids from Ministry of Education, Culture, Sports, Science, and Technologies of Japan (18H05222, 18J11010, 19H05069, 19K14753, 20H05847, 21K13954, and 24K00674). The authors acknowledge the financial support by JSPS and MAEE under the Japan-France integrated action program (SAKURA: 25765VC). Y.O. acknowledges NAOJ for the ALMA Joint Scientific Research Program (2024-27B). Y.O. also thanks NAOJ for the support as the ALMA 10th Anniversary Award. D.J. is supported by NRC Canada and by an NSERC Discovery Grant. L.P. and C. C. acknowledge financial support under the National Recovery and Resilience Plan (NRRP), Mission 4, Component 2, Investment 1.1, Call for tender No. 104 published on 2.2.2022 by the Italian Ministry of University and Research (MUR), funded by the European Union - NextGenerationEU - Project Title 2022JC2Y93 ChemicalOrigins: linking the fossil composition of the solar system with the chemistry of protoplanetary disks - CUP J53D23001600006 - Grant Assignment Decree No. 962 adopted on 30.06.2023 by the Italian Ministry of University and Research (MUR). L.P., C.C., G.S., and N.B. also acknowledge the EC H2020 project “Astro-Chemical Origins” (ACO, No 811312), the PRIN-MUR 2020 BEYOND-2p (Astrochemistry beyond the second period elements, Prot. 2020AFB3FX), the project ASI-Astrobiologia 2023 MIGLIORA (Modeling Chemical Complexity, F83C23000800005), the INAF-GO 2023 fundings PROTO-SKA (Exploiting ALMA data to study planet forming disks: preparing the advent of SKA, C13C23000770005), the INAF-Minigrant 2022 “Chemical Origins” (P.I.: L. Podio), and the INAF-Minigrant 2023 TRIESTE (“TRacing the chemical hEritage of our originS: from proTostars to plan- Ets”; PI: G. Sabatini). L.L. acknowledges the support of UNAM-DGAPA PAPIIT grants IN112820 and IN108324 and CONAHCYT-CF grant 263356. This project has received funding from the European Research Council (ERC) under the European Union Horizon Europe research and innovation program (grant agreement No. 101042275, project Stellar-MADE). S.V. and M.B. acknowledge support from the ERC under the European Union’s Horizon 2020 Research and innovation programme MOPPEX

833460. G.S. also acknowledges support from the INAF-Minigrant 2023 TRIESTE (“TRacing the chemical hEritage of our originS: from proTostars to planEts”; P.I.: G. Sabatini). I.J.-S acknowledges funding from grant Nos. PID2019-105552RB-C41 and PID2022-136814NB-I00 from the Spanish Ministry of Science and Innovation/State Agency of Research MCIN/AEI/10.13039/501100011033 and by “ERDF A way of making Europe.” E.B. acknowledges the Deutsche Forschungsgemeinschaft (DFG, German Research Foundation) under Germany’s Excellence Strategy—EXC 2094—390783311. S.B.C was supported by the NASA Planetary Science Division Internal Scientist Funding Program through the Fundamental Laboratory Research work package (FLaRe). E.B. acknowledges contribution of the Next Generation EU funds within the National Recovery and Resilience Plan (PNRR), Mission 4 - Education and Research, Component 2 - From Research to Business (M4C2), Investment Line 3.1 - Strengthening and creation of Research Infrastructures, Project IR0000034 - “STILES - Strengthening the Italian Leadership in ELT and SKA”. F.Me. acknowledges funding from the ERC under the EU’s Horizon Europe research and innovation program (grant agreement No. 101053020, project Dust2Planets).

Appendix Non-LTE Analysis for SO

To confirm whether the results obtained by the LTE (local thermodynamic equilibrium) analysis for SO (see Figure 4(b); Section 3.2) are reasonable, we conduct a non-LTE analysis. The non-LTE analysis is performed for five picked-up positions (A–E), unlike the pixel-based method for the calculation of the rotational temperature of SO.

We use the ^{34}SO ($J_N = 5_6 - 4_5$) line data in the non-LTE analysis in addition to the two SO ($J_N = 6_5 - 5_4$, $J_N = 6_6 - 5_5$) lines for accurate determination of the gas kinetic temperature. Figure 3 shows the spectra of these three lines at positions A–E. Although the ^{34}SO emission is much fainter than the SO emission, it is detected toward positions A–D with an S/N ratio higher than 6. Meanwhile, the detection of the ^{34}SO emission is marginal at position E, where the S/N ratio is 3.6. The parameters of the spectra are summarized in Table 4. The ^{34}SO line is frequency-diluted, since it is observed with a coarse-resolution backend (1.129 MHz). Hence, its peak intensity at each position is derived from the integrated intensity divided by the averaged line width of the two SO lines.

We conduct the non-LTE modeling and constrain the gas kinetic temperature, the SO column density, and the H_2 number density by the χ^2 method. We employed the escape probability for a static, spherically symmetric, and homogeneous medium (D. E. Osterbrock & G. J. Ferland 2006; F. F. S. van der Tak et al. 2007). We employ the energy levels, the Einstein A coefficients, and the state-to-state collisional rates of SO by T. J. Price et al. (2021). The energy levels and the Einstein A coefficients of ^{34}SO are taken from CDMS (H. S. P. Müller et al. 2005; C. P. Endres et al. 2016). We employ H_2 as the collision partner.⁵³ Since the collisional rates of ^{34}SO are not available, we employ those of SO as substitutes without any corrections. We assume the ratio of $N(^{32}\text{SO})/N(^{34}\text{SO})$ to be 19 in this calculation (R. Lucas & H. Liszt 1998).

⁵³ The ortho-to-para ratio of H_2 is assumed to be 3 in this calculation. We confirmed that the results do not change significantly by using an ortho-to-para ratio of 0.

In the χ^2 analysis, the SO and ^{34}SO data are treated simultaneously in the χ^2 analysis. Thus, the χ^2 value is calculated by the following equation:

$$\chi^2 = \sum_i \left(\frac{T_i^{\text{obs}} - T_i^{\text{calc}}}{\sigma_i} \right)^2, \quad (\text{A1})$$

where the summation is taken over the two SO and one ^{34}SO lines. T_i^{obs} and T_i^{calc} denote the observed and calculated peak temperatures. σ_i stands for the error of the observed temperature, which is calculated from two times the rms noise level of each spectrum and 10% of the intensity calibration error. T_i^{obs} and its rms are summarized in Table 4.

In the analysis, we scan wide ranges of parameter values to find the best-fit parameter values: every 2.5 K from 30–117.5 K for the gas kinetic temperature, every $0.25 \times 10^{14} \text{ cm}^{-2}$ from $8\text{--}13.75 \times 10^{14} \text{ cm}^{-2}$ for the SO column density, and every 1.5 times from $3 \times 10^5\text{--}5.05 \times 10^9 \text{ cm}^{-3}$ for the H_2 number density. The results are summarized in Table 5. The error values denote the range of the parameter value that corresponds to the above intensity error.

At position A (the interaction position of the outflow and the southern ridge component), the gas kinetic temperature is derived to be 55_{-14}^{+39} K. The relatively high temperature derived for Position A indicates that the shock heating is indeed occurring there, as discussed in Section 4.1. The gas kinetic temperatures are evaluated to be >23 K, 26_{-3}^{+15} , and >16 K at positions B, C, and D in the southern ridge, respectively. Although only the lower limits are obtained for positions B and D, the gas kinetic temperature tends to decrease as leaving from position A, and also from the protostar, along the southern ridge; however, it is still higher than 16 K at position D, which is the end of the southern ridge.

Only the lower limit is available for the gas kinetic temperature at position E. Since the ^{34}SO emission is marginally seen, the constraint on the parameters is rather loose (Table 5). Nevertheless, the high temperature (>56 K) condition is indeed confirmed, as suggested by the rotational temperature of SO (Figure 4). This result supports the local heating occurring at position E, as well as the result for position A; the heating mechanism is likely attributed to the bow shock at position E, as discussed in Section 4.2.

ORCID iDs

Yoko Oya  <https://orcid.org/0000-0002-0197-8751>
 Claire J. Chandler  <https://orcid.org/0000-0002-7570-5596>
 Eleonora Bianchi  <https://orcid.org/0000-0001-9249-7082>
 Tomoyuki Hanawa  <https://orcid.org/0000-0002-7538-581X>
 Yuri Aikawa  <https://orcid.org/0000-0003-3283-6884>
 Francois Dulieu  <https://orcid.org/0000-0001-6981-0421>

References

Andrews, S. M., Huang, J., Pérez, L. M., et al. 2018, *ApJL*, 869, L41
 Arce, H. G., Santiago-García, J., Jørgensen, J. K., et al. 2008, *ApJL*, 681, L21
 Arce, H. G., & Sargent, A. I. 2006, *ApJ*, 646, 1070
 Artur de la Villarmois, E., Guzmán, V. V., Jørgensen, J. K., et al. 2022, *A&A*, 667, A20
 Artur de la Villarmois, E., Jørgensen, J. K., Kristensen, L. E., et al. 2019, *A&A*, 626, A71
 Bachiller, R. 1996, *ARA&A*, 34, 111
 Bachiller, R., & Pérez Gutiérrez, M. 1997, *ApJL*, 487, L93
 Bachiller, R., Pérez Gutiérrez, M., Kumar, M. S. N., et al. 2001, *A&A*, 372, 899

Bacmann, A., Lefloch, B., Ceccarelli, C., et al. 2003, *ApJL*, 585, L55
 Bally, J. 2016, *ARA&A*, 54, 491
 Bianchi, E., Ceccarelli, C., Codella, C., et al. 2022, *A&A*, 662, A103
 Bianchi, E., López-Sepulcre, A., Ceccarelli, C., et al. 2023, *FaDi*, 245, 164
 Blandford, R. D., & Payne, D. G. 1982, *MNRAS*, 199, 883
 Bonnarel, F., Fernique, P., Bienaymé, O., et al. 2000, *A&AS*, 143, 33
 Bussmann, R. S., Wong, T. W., Hedden, A. S., et al. 2007, *ApJL*, 657, L33
 CASA Team, Bean, B., Bhatnagar, S., et al. 2022, *PASP*, 134, 114501
 Caselli, P., Hartquist, T. W., & Havnes, O. 1997, *A&A*, 322, 296
 Ceccarelli, C., Bacmann, A., Boogert, A., et al. 2010, *A&A*, 521, L22
 Ceccarelli, C., Boogert, A. C. A., Tielens, A. G. G. M., et al. 2002, *A&A*, 395, 863
 Ceccarelli, C., Caselli, P., Fontani, F., et al. 2017, *ApJ*, 850, 176
 Codella, C., Bianchi, E., Podio, L., et al. 2021, *A&A*, 654, A52
 Codella, C., Ceccarelli, C., Chandler, C., et al. 2021, *FrASS*, 8, 227
 Codella, C., Lefloch, B., Ceccarelli, C., et al. 2010, *A&A*, 518, L112
 Codella, C., Podio, L., De Simone, M., et al. 2024, *MNRAS*, 528, 7383
 Cosentino, G., Jiménez-Serra, I., Caselli, P., et al. 2019, *ApJL*, 881, L42
 Curtis, E. I., Richer, J. S., Swift, J. J., et al. 2010, *MNRAS*, 408, 1516
 Denis-Alpizar, O., Stoecklin, T., Dutrey, A., et al. 2020, *MNRAS*, 497, 4276
 Endres, C. P., Schlemmer, S., Schilke, P., et al. 2016, *JMoSp*, 327, 95
 Enoch, M. L., Evans, N. J., Sargent, A. I., et al. 2009, *ApJ*, 692, 973
 Feng, S., Beuther, H., Zhang, Q., et al. 2016, *ApJ*, 828, 100
 Fischer, W. J., Hillenbrand, L. A., Herczeg, G. J., et al. 2023, in ASP Conf. Ser. 534, Protostars and Planets VII, ed. S. Inutsuka et al. Vol. 534 (San Francisco: ASP), 355
 Gustafsson, M., Ravkilde, T., Kristensen, L. E., et al. 2010, *A&A*, 513, A5
 Hartmann, L. 2008, in *Accretion Processes in Star Formation*, ed. L. Hartmann (Cambridge: Cambridge Univ. Press)
 Hatchell, J., Fuller, G. A., & Richer, J. S. 2007, *A&A*, 472, 187
 Herczeg, G. J., Johnstone, D., Mairs, S., et al. 2017, *ApJ*, 849, 43
 Hirota, T., Machida, M. N., Matsushita, Y., et al. 2017, *NatAs*, 1, 0146
 Imai, M., Oya, Y., Svoboda, B., et al. 2022, *ApJ*, 934, 70
 Imai, M., Sakai, N., Oya, Y., et al. 2016, *ApJL*, 830, L37
 Larson, R. B. 2003, *RPPH*, 66, 1651
 Lee, C.-F., Mundy, L. G., Reipurth, B., et al. 2000, *ApJ*, 542, 925
 Lee, Y.-H., Johnstone, D., Lee, J.-E., et al. 2020, *ApJ*, 903, 5
 Lee, Y.-H., Johnstone, D., Lee, J.-E., et al. 2021, *ApJ*, 920, 119
 Le Gal, R., Öberg, K. I., Huang, J., et al. 2020, *ApJ*, 898, 131
 Lindberg, J. E., Jørgensen, J. K., Watanabe, Y., et al. 2015, *A&A*, 584, A28
 Lommen, D., Jørgensen, J. K., van Dishoeck, E. F., et al. 2008, *A&A*, 481, 141
 Lucas, R., & Liszt, H. 1998, *A&A*, 337, 246
 Machida, M. N., & Basu, S. 2019, *ApJ*, 876, 149
 Machida, M. N., & Hosokawa, T. 2013, *MNRAS*, 431, 1719
 Machida, M. N., Inutsuka, S.-ichiro., & Matsumoto, T. 2008, *ApJ*, 676, 1088
 Mairs, S., Lee, S., Johnstone, D., et al. 2024, *ApJ*, 966, 215
 Matsushita, Y., Takahashi, S., Machida, M. N., et al. 2019, *ApJ*, 871, 221
 Maureira, M. J., Gong, M., Pineda, J. E., et al. 2022, *ApJL*, 941, L23
 Mikami, H., Umemoto, T., Yamamoto, S., et al. 1992, *ApJL*, 392, L87
 Miotello, A., Testi, L., Lodato, G., et al. 2014, *A&A*, 567, A32
 Müller, H. S. P., Schlöder, F., Stutzki, J., et al. 2005, *JMoSt*, 742, 215
 Nakamura, F., Kamada, Y., Kamazaki, T., et al. 2011, *ApJ*, 726, 46
 Nakamura, F., & Li, Z.-Y. 2014, *ApJ*, 783, 115
 Nakamura, F., Sugitani, K., Shimajiri, Y., et al. 2011, *ApJ*, 737, 56
 Öbner, K. I., Guzmán, V. V., Walsh, C., et al. 2021, *ApJS*, 257, 1
 Offner, S. S. R., & Chaban, J. 2017, *ApJ*, 847, 104
 Ohashi, N., Saigo, K., Aso, Y., et al. 2014, *ApJ*, 796, 131
 Ohashi, S., Claudio, C., Sakai, N., et al. 2022, *ApJ*, 927, 54
 Okoda, Y., Oya, Y., Francis, L., et al. 2021, *ApJ*, 910, 11
 Omura, M., Tokuda, K., & Machida, M. N. 2024, *ApJ*, 963, 72
 Ortiz-León, G. N., Loinard, L., Kounkel, M. A., et al. 2017, *ApJ*, 834, 141
 Osterbrock, D. E., & Ferland, G. J. 2006, in *Astrophysics of Gaseous Nebulae and Active Galactic Nuclei*, 2nd. ed., ed. D. E. Osterbrock & G. J. Ferland (Sausalito, CA: Univ. Science Books), 2006
 Oya, Y. 2022, *A Few Tens au Scale Physical and Chemical Structures Around Young Low-Mass Protostars* (Singapore: Springer)
 Oya, Y., Kibukawa, H., Miyake, S., et al. 2022, *PASP*, 134, 094301
 Oya, Y., López-Sepulcre, A., Sakai, N., et al. 2019, *ApJ*, 881, 112
 Oya, Y., Moriwaki, K., Onishi, S., et al. 2018a, *ApJ*, 854, 96
 Oya, Y., Sakai, N., Lefloch, B., et al. 2015, *ApJ*, 812, 59
 Oya, Y., Sakai, N., López-Sepulcre, A., et al. 2016, *ApJ*, 824, 88
 Oya, Y., Sakai, N., Sakai, T., et al. 2014, *ApJ*, 795, 152
 Oya, Y., Sakai, N., Watanabe, Y., et al. 2017, *ApJ*, 837, 174
 Oya, Y., Sakai, N., Watanabe, Y., et al. 2018b, *ApJ*, 863, 72
 Oya, Y., Watanabe, Y., López-Sepulcre, A., et al. 2021, *ApJ*, 921, 12
 Oya, Y., & Yamamoto, S. 2020, *ApJ*, 904, 185

- Palla, F., & Stahler, S. W. 1991, *ApJ*, 375, 288
- Podio, L., Codella, C., Lefloch, B., et al. 2017, *MNRAS*, 470, L16
- Price, T. J., Forrey, R. C., Yang, B., et al. 2021, *JChPh*, 154, 034301
- Rocha, W. R. M., & Pilling, S. 2018, *MNRAS*, 478, 5190
- Sato, A., Tokuda, K., Machida, M. N., et al. 2023, *ApJ*, 958, 102
- Schilke, P., Walmsley, C. M., Pineau des Forets, G., et al. 1997, *A&A*, 321, 293
- Schöier, F. L., van der Tak, F. F. S., van Dishoeck, E. F., et al. 2005, *A&A*, 432, 369
- Sekimoto, Y., Tatematsu, K., Umemoto, T., et al. 1997, *ApJL*, 489, L63
- Sugimura, M., Yamaguchi, T., Sakai, T., et al. 2011, *PASJ*, 63, 459
- Tanius, M., Le Gal, R., Neri, R., et al. 2024, *A&A*, 687, A92
- Tokuda, K., Onishi, T., Saigo, K., et al. 2014, *ApJL*, 789, L4
- Tomisaka, K. 2000, *ApJL*, 528, L41
- Valdivia-Mena, M. T., Pineda, J. E., Segura-Cox, D. M., et al. 2022, *A&A*, 667, A12
- van der Marel, N., Kristensen, L. E., Visser, R., et al. 2013, *A&A*, 556, A76
- van der Tak, F. F. S., Black, J. H., Schöier, F. L., et al. 2007, *A&A*, 468, 627
- van der Wiel, M. H. D., Jacobsen, S. K., Jørgensen, J. K., et al. 2019, *A&A*, 626, A93
- Wakelam, V., Herbst, E., Loison, J.-C., et al. 2012, *ApJS*, 199, 21
- Warmels, R., Biggs, A., Cortes, P. A., et al. 2018, ALMA Technical Handbook, ALMA Doc. 6.3, ver. 1.0 (San Pedro de Atacama: ALMA) <https://almascience.nrao.edu/documents-and-tools/cycle6/alma-technical-handbook>
- Watanabe, Y., Sakai, N., Lindberg, J. E., et al. 2012, *ApJ*, 745, 126
- Wilking, B. A., & Lada, C. J. 1983, *ApJ*, 274, 698
- Ybarra, J. E., Barsony, M., Haisch, K. E., et al. 2006, *ApJL*, 647, L159
- Yoon, S.-Y., Herczeg, G. J., Lee, J.-E., et al. 2022, *ApJ*, 929, 60
- Zapata, L. A., Ho, P. T. P., Schilke, P., et al. 2009, *ApJ*, 698, 1422
- Ziurys, L. M., Friberg, P., & Irvine, W. M. 1989, *ApJ*, 343, 201